SCOTCH – search for clandestine optically thick compact H II regions: II

A. L. Patel [🄳],[1]⋆ J. S. Urquhart [🄳],[1]⋆ A. Y. Yang,[2,3]⋆ T. Moore,[4] M. A. Thompson,[5] K. M. Menten[6] and T. Csengeri[7]

[1]*Centre for Astrophysics and Planetary Science, University of Kent, Canterbury CT2 7NH, UK*
[2]*National Astronomical Observatories, Chinese Academy of Sciences, A20 Datun Road, Chaoyang District, Beijing 100101, P. R. China*
[3]*Key Laboratory of Radio Astronomy and Technology, Chinese Academy of Sciences, A20 Datun Road, Chaoyang District, Beijing 100101, P. R. China*
[4]*Astrophysics Research Institute, Liverpool John Moores University, Liverpool Science Park, 146 Brownlow Hill, Liverpool L3 5RF, UK*
[5]*School of Physics and Astronomy, University of Leeds, Leeds LS2 9JT, UK*
[6]*Max Planck Institute for Radio Astronomy, Auf dem Hügel 69, D-53121 Bonn, Germany*
[7]*Laboratoire d'astrophysique de Bordeaux, Univ. Bordeaux, CNRS, B18N, allée Geoffroy Saint-Hilaire, F-33615 Pessac, France*

ABSTRACT

In this study we present $18-24$ GHz and high-angular-resolution (0.5 arcsec) radio wavelength Australia Telescope Compact Array follow-up observations towards a sample of 39 HC H II region candidates. These objects, taken from a sample hosting 6.7 GHz methanol masers, were chosen due to the compact and optically thick nature of their continuum emission. We have detected 27 compact radio sources and constructed their spectral energy distributions over the 5–24 GHz range to determine the young H II region's physical properties, i.e. diameter, electron density n_e, emission measure, Lyman continuum flux $N_{\rm Ly}$, and turnover frequency ν_t. The flux measurements are fitted for 20 objects assuming an ionization-bounded H II region with uniform density model. For the remaining seven objects that lack constraints spanning both their optically thick and thin regimes, we utilize relations from the literature to determine their physical properties. Comparing these determined parameters with those of known hypercompact (HC) and ultracompact (UC) H II regions, we have identified 13 HC H II regions, six intermediate objects that fall between HC H II and UC H II regions, six UC H II regions and one radio jet candidate which increases the known population of HC H II regions by $\sim$50 per cent. All the young and compact H II regions are embedded in dusty and dense clumps and $\sim$80 per cent of the HC H II regions identified in this work are associated with various maser species (CH$_3$OH, H$_2$O, and OH). Four of our radio sources remain optically thick at 24 GHz; we consider these to be among the youngest HC H II regions.

Key words: stars: evolution – stars: formation – HII regions – radio continuum: stars.

1 INTRODUCTION

Massive stars ($>8\,{\rm M_\odot}$, $>10^4\,{\rm L_\odot}$) generate intense Lyman continuum emissions with sufficient energy to ionize their surroundings, resulting in the formation of H II regions. These hot bubbles of dense ionized gas are overpressured with respect to their surrounding medium and hence expand over time. Their expansion drives ionization shocks that propagate into the ambient medium (Dyson, Williams & Redman 1995). The smallest and most compact H II regions are naturally assumed to be the youngest; however, many details of their evolution and formation remain unclear. An important question that remains unresolved in the formation of H II regions is how accretion proceeds against the outward pressure within the ionization front.

Many theoretical models have predicted the outcome for the formation and evolution of H II regions. For example, the McKee & Tan (2003) turbulent core and Peters et al. (2010) ionization feedback models suggest that the youngest H II regions expand into outflow-driven cavities away from the disc accretion flows. This implies

that the expansion of young H II regions does not halt the accretion flow on to young high-mass star. A similar result has been reported in Keto (2007) who suggests that while the young high-mass star grows, emitting an increasing amount of ionizing UV photons, the surrounding H II region goes through a three-stage evolutionary sequence: non-existent/quenched, bipolar outflow, and spherical outflows. Contrary to this, the models of Hosokawa & Omukai (2009) and Hosokawa, Yorke & Omukai (2010) suggest that the high accretion rates of material falling on to massive stars cause the protostar to bloat and swell (and pulsate). This reduces the effective temperature of the star and delays the development of an H II region. It is clear that the main differences in these theoretical models arise at the initial stage of H II region development. Investigating the physical characteristics of the youngest and smallest H II regions is crucial to understand their initial conditions and constrain theoretical models.

The two youngest H II region stages are commonly known as hypercompact H II (HC H II) and ultracompact H II (UC H II) regions (Kurtz & Hofner 2005). HC H II regions are the youngest and are defined by the following physical parameters: physical diameter ≤ 0.05 pc, an electron density (n_e) of $\geq 10^5$ cm^{-3}, and an emission measure of $\geq 10^8$ pc cm^{-6}. The brightest HC H II regions are associated with radio recombination line (RRL) linewidths of $\Delta V \geq$

⋆ E-mails: alp48@kent.ac.uk (ALP); j.s.urquhart@kent.ac.uk (JSU); ayyang@mpifr-bonn.mpg.de (AYY)

40 km s^{-1} (Kurtz et al. 1999; Sewilo et al. 2004; Hoare et al. 2007; Murphy et al. 2010). The next evolutionary phase is the UC H II region; these have typical diameters of ≤ 0.1 pc, an n_e of $\geq 10^4$ cm^{-3}, an emission measure of $\geq 10^7$ pc cm^{-6}, and RRL linewidths $\Delta V \geq \sim 25$–30 km s^{-1} (Wood & Churchwell 1989; Afflerbach et al. 1996; Hoare et al. 2007).

HC H II regions are particularly interesting in the study of massive star formation because they are thought to exhibit a size scale suitable for a single high-mass star (or a binary system), in contrast to ultracompact (UC) or compact H II regions, which are more likely to harbour clusters of massive stars (e.g. Kurtz 2000; Hoare et al. 2007). Theoretical models suggest that O-type stars form gradually via accretion through an HC H II region on to intermediate-mass B stars (Keto 2007). However, this has yet to be definitively confirmed. Thus, the study of HC H II regions is important to understand the evolution of massive stars. The differences between these two evolutionary classes are somewhat arbitrary as the evolution from the HC H II region stage to the UC H II region stage is thought to be continuous (Garay & Lizano 1999; Yang et al. 2019). Currently the number of known HC H II regions is small and a larger sample with good statistics is needed to constrain the properties of this very early stage of massive star formation.

To date, only 23 HC H II regions have been identified based on their emission nature at centimetre, infrared, and submillimetre wavelengths (Yang et al. 2019; Yang et al. 2021 and references therein). These HC H II regions were selected based on their rising spectral index at 5 GHz. Young H II regions are deeply embedded and heavily obscured by thick cocoons of molecular gas that are opaque in the optical and near-infrared regimes; however, they are transparent to radio emission. We can therefore use radio-continuum observations to detect these regions and characterize their properties. The objective of this study is to investigate and confirm the nature of a sample of early-stage H II regions identified in Patel et al. (2023) (hereafter Paper I) and is specifically aimed at increasing the sample of HC H II regions.

In Paper I, we have presented a detailed analysis of high-frequency (i.e. 23.7 GHz) radio-continuum emission towards 141 sources associated with 6.7-GHz class II methanol masers, as identified by the Methanol MultiBeam survey (MMB; Green et al. 2009). Paper I used archival data taken with the Australia Telescope Compact Array (ATCA) by Titmarsh et al. (2016). Class II Methanol masers are known to be exclusively associated with the early stages of high-mass star formation (Breen et al. 2013), and are therefore an ideal place to search for HC H II regions. This low-resolution ($\sim$20-arcsec) study detected 68 compact radio sources. We conducted a multiwavelength analysis of these objects and identified 49 H II regions, of which the emission of 13 are optically thick between 5 and 23.7 GHz.

In this paper we report the results of high-angular-resolution ($\sim$0.5-arcsec) observations towards the sample of 39 compact (i.e. y-factor ($f_{\rm int}/f_{\rm peak}$) < 2)[1] and/or optically thick ($\alpha > 0.5$) H II regions identified in Paper I. We derive the physical properties for each radio source and classify their properties into three types: HC H II regions, UC H II regions, and intermediate transition objects that are between the HC H II and UC H II regions stages. The structure of the paper is as follows: the observations, data reduction, imaging, and source extraction methods are described in Section 2. Section 3 presents the results, a discussion of the physical parameters, and the methods used to derive them. In Section 4, we investigate the evolution of H II regions by comparing our sample with known compact H II

regions. We divide our H II regions into sub classes based on their physical properties and discuss the youngest H II regions within our sample. We summarize our results and highlight our main findings in Section 5.

2 OBSERVATIONS AND DATA REDUCTION

2.1 Observational set-up

The ATCA is an array of six 22-m antennas located 500 km north–west of Sydney, in the Paul Wild Observatory. Five of these antennas can move along a 3-km long east–west track or a 214-m north spur. The sixth antenna is fixed, being located out 6 km along the east–west track. The ATCA is an Earth-rotation aperture-synthesis radio interferometer and has 17 standard configurations that are designed to give optimum and minimum-redundancy coverage of the visibilities (u, v) plane after a 12-h observing period. The observations presented here were collected over 4 d in 2022 April towards 39 fields between Galactic longitudes $2°-18°$ and $326°-340°$. These fields were selected towards radio sources that are either found unresolved or optically thick at 23.7 GHz based on the low-resolution observations (20 arcsec) presented in Paper I.

The observations were made using the 6-km configuration (6A), utilizing all six antennae in a linear orientation with the shortest and longest baselines being 337 and 5939 m, respectively. The Compact Array Broad-band Backend (CABB; Wilson et al. 2011) was configured with 2×2-GHz continuum bands with 32×64-MHz channels to observe at 18 and 24 GHz simultaneously. The primary beam for the ATCA has a full width at half-maximum (FWHM) size of 2.6 arcmin and the synthesized beam of the 6A antenna configuration is ~ 0.4 arcsec (FWHM) at 24 GHz. We simultaneously measured five zoom windows at 17.3, 18.0, 18.7, 23.4, and 24.5 GHz targeting the H72α, H71α, H70α, H65α, and H64α RRLs, respectively (Brown, Lockman & Knapp 1978). Here we present the results obtained from the 2 GHz continuum bands centred at 18 and 24 GHz; the results from the RRL observations will be presented in a future paper. Target sources were divided into four blocks based on their position, and observations of each field typically consisted of six 1.5-min integration cuts that were spaced over a range of hour angles to maximize the uv coverage. The total on-source integration time of $\sim$10 min gives a theoretical rms noise of $\sim$0.1 mJy beam^{-1} at both frequencies, which is sufficient to detect a B0.5 or earlier type star embedded within an ionized nebula at a distance of 20 kpc (Giveon et al. 2005; Urquhart et al. 2007b).

The observations were generally carried out over a 10 h period to provide even uv-coverage; however, for higher declination sources (i.e. close to the celestial equator $l = 2°- 18°$) the observations were limited to a 5 h period. The synthesized beams for sources at higher declination are relatively poor given that the ATCA is an E-W interferometer. Consequently, the major axis of the beam is

Table 1. The CABB theoretical sensitivities for 18 and 24 GHz, respectively. The synthesized beam is presented as beam major × beam minor. The noise values have been estimated assuming 10 min on-source integration time and stable weather conditions.

Target group	Average declination (°)	Synthesized beam 18 GHz (arcsec)	24 GHz (arcsec)	Theoretical RMS 18 GHz (mJy beam^{-1})	24 GHz (mJy beam^{-1})
1	−52	0.61 × 0.48	0.46 × 0.36	0.094	0.160
2	−46	0.67 × 0.48	0.50 × 0.36	0.094	0.160
3	−25	1.14 × 0.48	0.86 × 0.36	0.098	0.166
4	−15	2.66 × 0.48	1.41 × 0.36	0.100	0.168

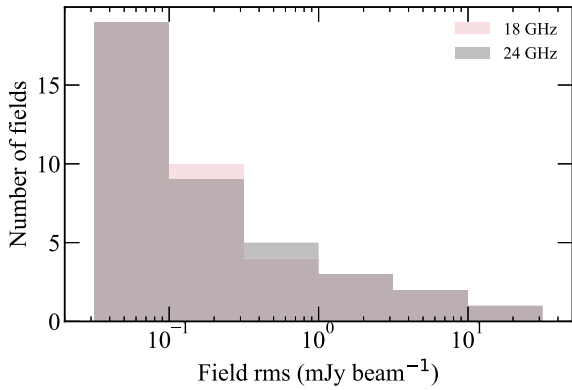[1]The y-factor is the ratio of integrated to peak flux density.

Figure 1. Histogram of the number of fields observed as a function of the map rms noise at both frequencies. The data have been binned using a value of 0.5 dex.
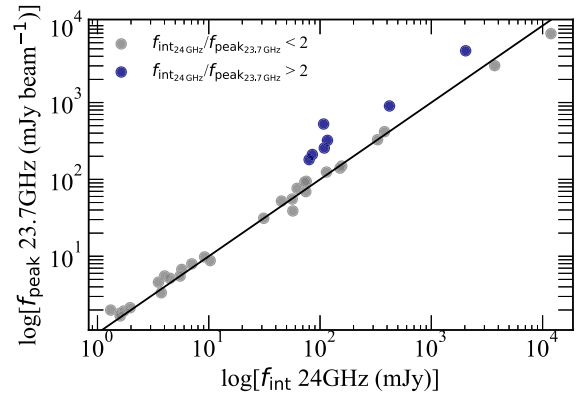

Figure 2. Distribution of the integrated flux density at 24 GHz from this study against the peak flux densities at 23.7 GHz in Paper I for the detected radio sources. Sources shown as blue circles are probably affected by spatial filtering. The solid black line represents the line of equality.

significantly elongated (average aspect ratio $\sim 5{:}1$). Table 1 provides the theoretical size of the beam and Red MSX Source (RMS) of each group based on the average declination at 18 and 24 GHz, respectively. To correct for fluctuations in the phase and amplitude caused by atmospheric conditions, the sources were sandwiched between observations of a nearby phase calibrators. The primary ($1934-648$) and bandpass ($1252-055$) calibrator were observed once during each set of observation for approximately 10 min each, to allow the absolute calibration of the flux density and bandpass.

2.2 Data reduction and imaging

The calibration and reduction of these data were performed using the MIRIAD reduction package (Sault, Teuben & Wright 1995) following standard ATCA procedures. We performed a flagging procedure to eliminate any radio-frequency interference (RFI) and poor data. The procedure was performed iteratively, until all the RFI signals were removed from the visibility plots. The calibrated data were imaged and cleaned using the MIRIADCLEAN algorithm using a robust weighting of 0.5 and we set a limit of 200 cleaning components or until the first negative component was encountered. All our fields converged at the first negative component. Additionally, we corrected the primary beam using the LINMOS function to generate a final map. This resulted in an image size of 50×50 arcsec using a pixel size of ~ 0.2 arcsec. The final maps were made by combining the data sets for all 4 d to improve the *uv*-coverage and signal-to-noise ratio. In Fig. 1, we present a histogram of the rms noise of each field. The

rms noise levels were estimated from emission-free regions close to the centre of the reduced image. Median noise values are ~ 0.13 mJy beam^{-1}, which is consistent with the theoretical noise values. Due to the nature of interferometric observations, the largest well-imaged structures at 18 and 24 GHz are 5.5 and 4.0 arcsec, respectively. We present the observational parameters in Table 2.

2.3 Source parameters and final catalogue

The reduced maps were examined for compact, high surface brightness sources using a nominal 3σ detection threshold, where σ refers to the image rms noise level. The radio maps that had a peak flux density above the detection threshold were visually inspected to confirm the presence of the radio source and identify emission from over resolved sources and bright sidelobes.

In total, we have detected radio-continuum emission above 3σ in 35 of 39 observed fields, corresponding to a recovery rate of ~ 90 per cent. The radio emission consists of a single compact radio source in 22 fields; a further 12 fields contain a single extended radio source, and the remaining field contains two distinct radio sources. We have identified seven fields (i.e. G002.614+0.134, G011.937$-$0.616, G014.104+0.092, G331.130$-$0.243, G332.826$-$0.549, G333.163$-$0.100, G340.056-0.244) which display evidence of large-scale, overresolved emission (i.e. $f_{\mathrm{int}_{24\,\mathrm{GHz}}}/f_{\mathrm{peak}_{23.7\,\mathrm{GHz}}} > 2$). Each of these radio sources has a lower

Table 2. Observational parameters from all observed fields. The field names and pointing centres of the observations are based on the radio names and positions.

| Field name | RA (J2000) (h:m:s) | Dec. (J2000) (d:m:s) | Field rms | | Beam size 18 GHz | | | Beam size 24 GHz | | |
			18 GHz (mJy)	24 GHz (mJy)	Major (arcsec)	Minor (arcsec)	Position angle (°)	Major (arcsec)	Minor (arcsec)	Position angle (°)
G002.143+0.009	17:50:36.02	-27:05:46.9	0.1	0.1	1.8	0.5	-12.4	1.7	0.3	-11.1
G002.614+0.134	17:51:12.27	-26:37:38.8	0.2	0.2	1.9	0.5	-11.6	1.8	0.3	-10.4
G003.438$-$0.349	17:54:55.66	-26:09:47.4	0.1	0.2	2.0	0.5	-12.9	1.9	0.3	-11.2
G003.910+0.001	17:54:38.75	-25:34:44.7	0.5	0.4	2.1	0.5	-12.1	2.0	0.3	-10.5
G004.680+0.277	17:55:18.83	-24:46:29.5	0.1	0.1	2.2	0.5	-11.3	2.1	0.3	-10.0
G005.885$-$0.392	18:00:30.39	-24:04:00.1	15.9	16.6	2.2	0.5	-11.2	2.1	0.3	-9.9
G011.904$-$0.141	18:12:11.43	-18:41:29.4	0.3	0.3	3.8	0.4	-7.9	3.2	0.3	-7.3
G011.937$-$0.616	18:14:01.05	-18:53:24.9	1.1	1.9	3.8	0.4	-7.9	3.1	0.3	-7.4
G012.112$-$0.127	18:12:33.60	-18:30:06.8	0.1	0.1	4.0	0.4	-7.5	3.3	0.3	-7.0

Note. Only a small portion of the data is provided here; the full table is only available in electronic form.
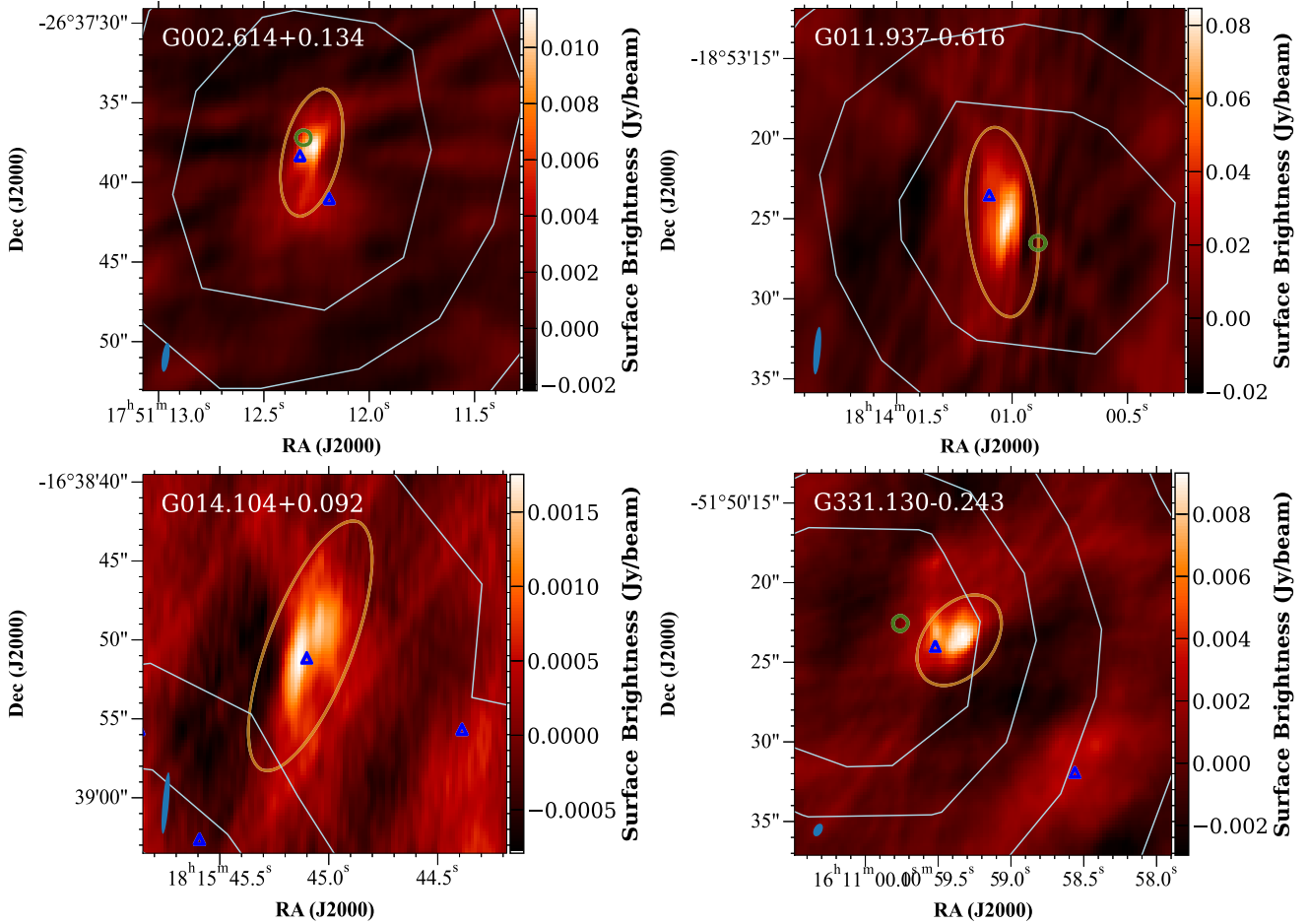
Figure 3. Examples of four radio fields that have been excluded. The remaining four fields can be found in Fig. A1 of the appendix. The orange ellipse shows the resultant fit to the radio emission and the green circles show the position of the methanol maser(s) located in the field. The blue triangles show the position of any low-frequency (5-GHz) radio counterparts. The grey contours trace the 870-μm dust emission from ATLASGAL (Schuller et al. 2009). The filled blue ellipse in the bottom left-hand corner of each image indicates the size and orientation of the synthesized beam.

integrated flux density at 18 and 24 GHz when compared with the low-resolution 23.7-GHz peak flux density of Paper I, suggesting a loss of flux in the high-resolution maps as a result of spatial filtering.

Fig. 2 presents a comparison between the integrated flux densities at 24 GHz in this work and the peak flux densities at 23.7 GHz from Paper I. This plot shows that the majority of our radio sources cluster around the line of equality, demonstrating that there is no significant loss in flux density between the two spatial resolutions. The outliers (blue) correspond to the above seven overresolved radio sources that are removed from the final catalogue. We present maps of four of these sources in Fig. 3. The strong correlation of fluxes for the compact radio sources also indicates that there is little variability in the brightness of these sources over the 10 yr period between the high- and low-resolution observations.

In Section 2.1, we mentioned that, for the late-rising sources during the observations, the synthesized beam is significantly elongated. We identify five fields that fall within this category. This can be seen visually as the sources appear elongated and as a result we are unable to constrain the sizes accurately. Of the five fields identified, one field contains two radio sources (G014.604+0.016). The fluxes extracted from this region are unlikely to be reliable and so the two sources in this map are excluded from further analysis. The source,

G018.735−0.227, in the second field, shows the most significant elongation, and is reliably detected at 18 GHz (SNR = 9.5). However, at 24 GHz, we are unable to deconvolve the emission. In this case, we use the 18 GHz fit to estimate upper limits for the flux densities at 24 GHz. The remaining three fields are included, with a note indicating that the source sizes are less reliable.

There are four non-detections (G012.112−0.127, G014.229−0.510, G331.710+0.604, G338.280+0.542) in this study and these objects were weak detections at 23.7 GHz of Paper I (i.e. SNR < 3) with average noise values of ∼0.5 mJy beam^{-1}. Our high-frequency data provide better sensitivity (i.e. ∼0.08 mJy beam^{-1}). It is possible that these objects were false detections at 23.7 GHz in Paper I as a result of higher noise values. Alternatively, given our limited sensitivity to spatial scales greater than 5 arcsec, it is possible that the emission from these objects could have been filtered out, resulting in them not being detected in these data. Another possibility is that they are variable H II regions as discussed in Yang et al. (2023).

We use the MIRIAD task IMFIT to determine the positions, peak, and integrated flux densities and sizes of the remaining 27 compact radio detections. This was achieved by carefully drawing a polygon around the detection as an input to IMFIT where a two-component Gaussian is fitted around the emission.

Table 3. Extracted source parameters from our detected radio sources. Column 1 is the radio name, which is a combination of the Galactic longitudes and latitudes determined by fitting ellipsoidal Gaussian using IMFIT. Columns 2 and 3 are the right ascension and declination of each source, respectively. Columns 4–9 present 18-GHz source parameters and columns 10–16 present 24-GHz source parameters. Sources with a † indicate those with a poor synthesized beam. – are those for which sizes could not be deconvolved.

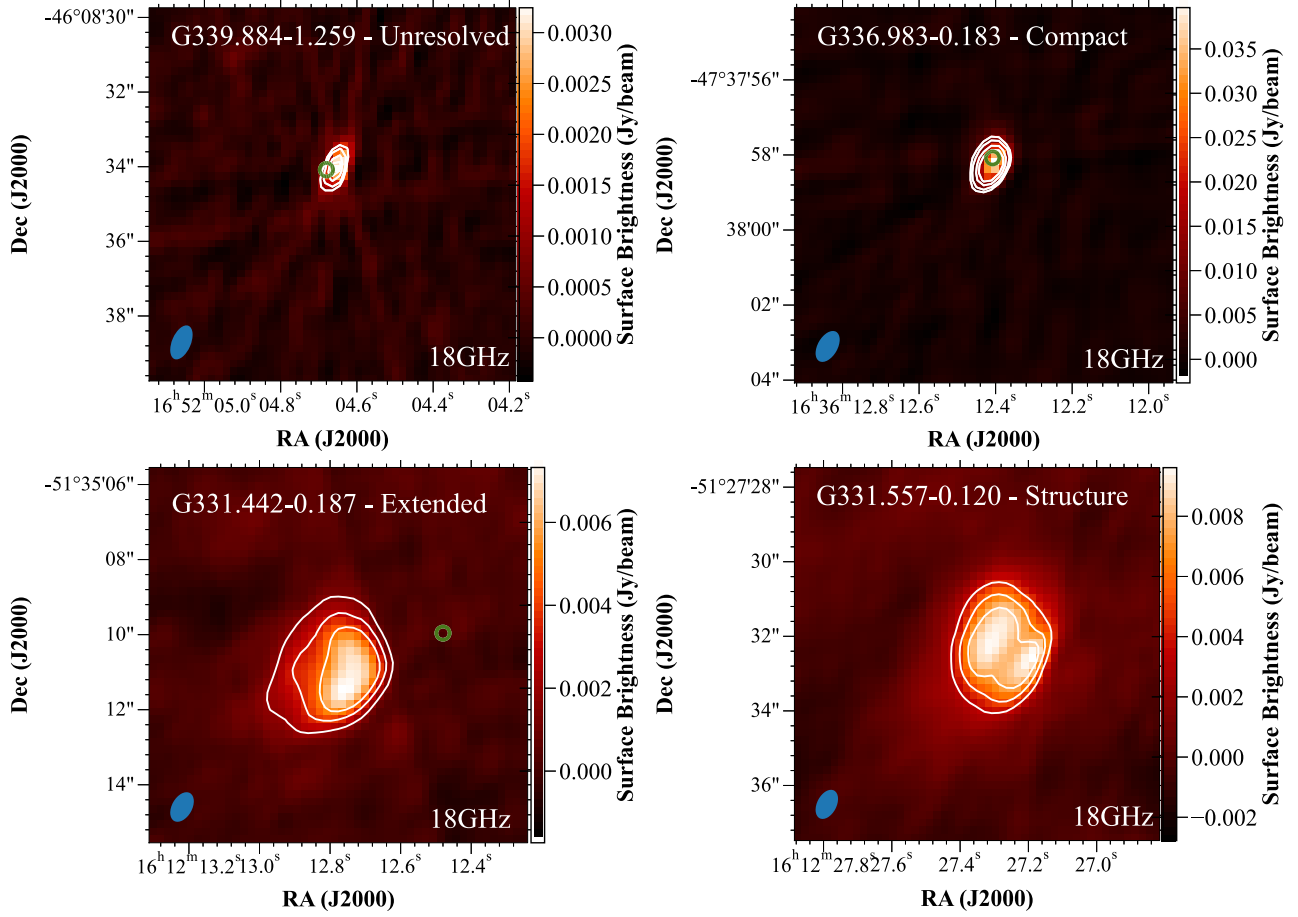| Radio name (1)	RA J2000 (h:m:s) (2)	Dec. J2000 (d:m:s) (3)	18GHz f_{peak} (mJy beam^{-1}) (4–5)	Δf_{peak}	f_{int} (mJy) (6–7)	Δf_{int}	$\theta_{maj} \times \theta_{min}$ (PA) (arcsec × arcsec (°)) (8–9)	$\theta_{maj_d} \times \theta_{min_d}$ (PA$_d$)	24GHz f_{peak} (mJy beam^{-1}) (10–11)	Δf_{peak}	f_{int} (mJy) (12–13)	Δf_{int}	$\theta_{maj} \times \theta_{min}$ (PA) (arcsec × arcsec (PA)) (14–15)	$\theta_{maj_d} \times \theta_{min_d}$ (PA$_d$)	θ_s (arcsec) (16)
G002.143+0.009†	17:50:36.02	−27:05:46.9	2.3	0.17	4.2	0.56	2.3 × 0.6 (−8.4)	1.5 × 0.4 (−8.1)	1.8	0.36	3.5	1.1	2.3 × 0.5 (−7.5)	1.5 × 0.3 (−3.3)	0.70
G003.438−0.349†	17:54:55.65	−26:09:47.4	9.1	0.58	89	13	4.1 × 2.1 (+0.1)	3.6 × 2.0 (+3.6)	5.2	0.36	75	13	4.2 × 1.9 (−0.9)	3.9 × 1.9 (+1.3)	2.70
G003.910+0.001†	17:54:38.75	−25:34:44.7	37	3.4	76	10	3.7 × 0.6 (−11)	3.0 × 0.3 (−10)	33	3.0	73	9.6	3.4 × 0.4 (−9.7)	2.7 × 0.3 (−9.2)	0.87
G004.680+0.277†	17:55:18.83	−24:46:29.5	6.5	0.64	9.8	1.4	3.3 × 0.5 (−9.8)	–	5.5	0.61	9.2	1.5	3.0 × 0.4 (−9.5)	2.2 × 0.2 (−9.1)	0.65
G005.885−0.392†	18:00:30.38	−24:04:00.5	470	49	15000	9200	6.8 × 4.5 (+57)	6.8 × 4.1 (+60)	280	32	12000	5400	6.5 × 4.0 (+31)	6.4 × 3.8 (+35)	4.90
G011.904−0.141†	18:12:11.43	−18:41:29.6	15	2.2	41	12	4.6 × 0.9 (−1.2)	3.5 × 0.7 (+1.5)	14	1.6	40	8.7	3.5 × 0.7 (−3.5)	2.4 × 0.6 (−1.9)	1.20
G012.199−0.034†	18:12:23.60	−18:22:53.5	6.4	0.49	54	8.2	5.7 × 2.1 (−1.6)	4.7 × 2.0 (+0.1)	3.5	0.24	57	14	7.2 × 1.9 (+2.8)	6.6 × 1.9 (+4.2)	3.50
G012.208−0.102†	18:12:39.69	−18:24:20.7	22	1.0	160	13	5.2 × 2.0 (−11)	4.1 × 1.9 (−16)	12	0.64	150	24	6.3 × 1.7 (−11)	5.7 × 1.7 (−12)	3.10
G018.461−0.004†	18:24:36.34	−12:51:05.3	64	5.1	390	70	7.5 × 1.6 (−3.0)	5.9 × 1.6 (−2.1)	37	4.2	380	120	10 × 1.3 (0.18)	9.3 × 1.2 (+1.3)	3.40
G018.665+0.029†	18:24:52.60	−12:39:20.0	2.2	0.18	5.9	0.86	6.1 × 0.9 (−2.7)	3.7 × 0.8 (+0.1)	1.5	0.16	5.5	1.0	6.5 × 0.8 (−3.1)	4.3 × 0.7 (−1.8)	1.80
G018.735−0.227†	18:25:56.47	−12:42:49.0	0.62	0.15	1.7	1.3	7.9 × 0.7 (−2.0)	6.2 × 0.5 (−0.6)	< 0.54	–	< 1.4	–	–	–	–
G326.475+0.703	15:43:16.62	−54:07:14.9	0.75	0.053	0.84	0.19	0.8 × 0.6 (−33)	–	1.2	0.36	2.0	1.1	0.8 × 0.4 (−25)	0.7 × 0.1 (−24)	0.27
G327.402+0.445	15:49:19.32	−53:45:14.4	41	1.6	120	6.9	1.6 × 0.9 (−17)	1.1 × 0.4 (−11)	30	2.3	110	13	1.4 × 0.7 (−13)	1.1 × 0.6 (−9.8)	0.80
G331.442−0.187	16:12:12.75	−51:35:10.9	7.2	0.34	78	9.9	2.5 × 2.0 (−23)	2.0 × 1.1 (−21)	3.8	0.2	75	8.2	2.7 × 1.8 (−29)	2.1 × 1.3 (−30)	1.70
G331.542−0.067	16:12:09.02	−51:25:47.5	130	5.1	320	18	1.3 × 0.9 (−37)	1.0 × 0.7 (−38)	80	4.1	330	25	1.3 × 0.8 (−25)	1.2 × 0.7 (−25)	0.91
G331.557−0.120	16:12:27.28	−51:27:32.4	11	0.33	170	7.4	3.0 × 2.3 (−25)	1.7 × 1.3 (−24)	6.1	0.29	160	13	3.1 × 2.2 (−19)	1.8 × 1.4 (−18)	1.60
G332.987−0.487	16:20:37.77	−50:43:49.6	6.4	0.78	9.2	1.7	1.1 × 0.6 (−15)	0.9 × 0.1 (−11)	7.0	1.1	12	2.9	0.9 × 0.5 (−9.2)	0.7 × 0.2 (+3.6)	0.36
G333.029−0.063	16:18:56.86	−50:23:54.2	15	1.6	25	3.7	1.2 × 0.6 (−22)	1.2 × 0.6 (−11)	13	1.7	31	6.7	1.2 × 0.6 (−11)	1.0 × 0.3 (−5.6)	0.59
G333.135−0.432	16:21:02.95	−50:35:12.6	360	25	3400	860	2.4 × 1.9 (+38)	2.4 × 1.7 (+40)	230	17	3700	770	2.8 × 1.6 (+6.0)	2.7 × 1.5 (+7.7)	2.05
G336.983−0.183	16:36:12.41	−47:37:58.3	39	1.5	52	3.0	0.8 × 0.3 (−25)	0.6 × 0.4 (−8.2)	33	2.4	56	6.0	1.0 × 0.5 (−16)	0.7 × 0.4 (−12)	0.52
G338.566+0.110	16:41:07.15	−46:15:30.4	1.6	0.091	9.7	0.91	2.1 × 1.5 (−16)	1.9 × 1.4 (−13)	9.8	0.081	10	1.5	2.4 × 1.3 (−7.9)	2.3 × 1.2 (−6.6)	1.71
G338.925+0.556	16:40:33.54	−45:41:37.6	1.1	0.15	1.4	0.33	1.3 × 0.6 (−15)	–	1.2	0.037	1.6	0.14	1.0 × 0.4 (−19)	0.5 × 0.2 (−22)	0.27
G339.282+0.136	16:43:43.08	−45:42:08.6	2.6	0.26	3.1	0.57	1.2 × 0.6 (−23)	0.7 × 0.3 (−24)	2.0	0.36	3.7	1.2	1.0 × 0.6 (−21)	0.6 × 0.4 (−31)	0.50
G339.622−0.121	16:46:06.00	−45:36:44.0	1.0	0.16	1.7	0.69	1.3 × 0.7 (−14)	0.9 × 0.4 (−5.5)	0.95	0.29	1.7	1.2	1.1 × 0.5 (−12)	0.8 × 0.3 (−7.4)	0.47
G339.681−1.207	16:51:06.22	−46:15:58.1	0.92	0.15	1.2	0.36	1.2 × 0.6 (−20)	0.9 × 0.2 (−16)	1.4	0.39	1.3	0.81	0.7 × 0.3 (−11)	0.8 × 0.2 (−26)	0.36
G339.884−1.259	16:52:04.65	−46:08:34.0	3.4	0.34	3.7	0.78	0.8 × 0.4 (−18)	–	4.3	0.54	5.7	1.3	0.9 × 0.4 (−12)	0.5 × 0.1 (+4.1)	0.26
G339.980−0.539	16:49:14.72	−45:36:32.4	44	2.5	110	9.0	1.5 × 0.9 (−14)	1.1 × 0.7 (−5.7)	28	1.1	100	6.0	1.4 × 0.7 (−9.4)	1.2 × 0.6 (−5.2)	0.86

Figure 4. Examples of four radio sources with different morphologies. The top left panel presents an unresolved radio source (G339.884−1.259), the top right is compact radio source G336.983−0.183, the bottom left panel shows an extended source (G331.442−0.187), and the bottom right shows a structured source (G331.557−0.120). The white contours of each map start at a level of 3σ and are equally spaced by 3σ. The orange ellipse shows the resultant fit from IMFIT to the radio emission and the green circles show the position of the methanol maser(s) located in the field. The filled blue ellipse in the bottom left-hand corner of each image indicates the size and orientation of the synthesized beam.
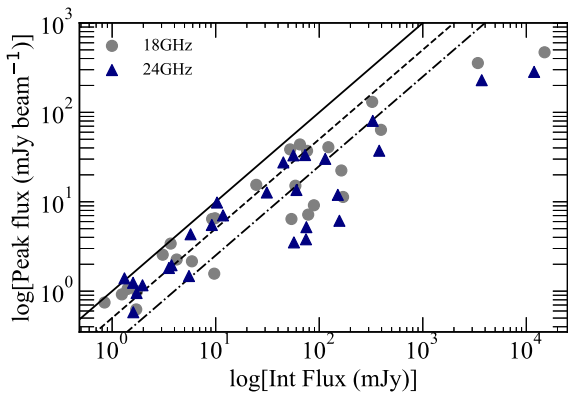
Figure 5. Distribution of the integrated flux density versus peak flux density for the 27 radio detections at 18 and 24 GHz. The solid line represents a line of equality where the flux densities are the same, indicating the radio source is unresolved. The dashed line represents a line with $y = 2$, suggesting the radio source is compact. The dash–dotted line has a y−factor of 4; sources with y−factors above this are considered to be extended.

3 RESULTS

3.1 Observational results

Our high-resolution catalogue is given in Table 3 and contains the extracted parameters for the 27 compact radio sources detected at 18 and 24 GHz. We present the radio name, RA, Dec., peak, and integrated flux densities and FWHM major, minor axis sizes and position angle in Columns 1−16 of Table 3. In Column 15, we present the deconvolved major and minor source sizes, along with the position angle, determined from IMFIT using the highest resolution map where the source is detected. Additionally, in Column 16 we provide the geometric deconvolved source size. Five radio detections are unresolved at 18 GHz; these are indicated as dashes in Table 3.

We categorize our sample of 27 radio detections into four morphologies: unresolved, compact, extended, and structured, and in Fig. 4 we present examples of each of these. The contouring highlights regions of low and high dynamic ranges, which enables us to differentiate between compact, bright radio emission and extended structures with low surface brightness. We have identified five sources that are unresolved at 18 GHz and have y-factors close to 1 (see the upper left panel of Fig. 4). A compact radio source is described to have a y−factor <2 and shows visual signs of extension but no structure (see lower left panel of Fig. 4). A further 11 sources

are identified as being extended. We find three radio sources that have complex substructure and an example is shown in the lower right panel of Fig. 4.

In Fig. 5, we present a scatter plot of the y−factor at 18 and 24 GHz for the 27 radio detections. Inspection of the plot reveals that the distribution is in agreement with the morphologies characterized above. In total, we have identified 14 radio sources that have a y−factor ≤2 that we have classified to be compact, and 13 radio sources that are extended.

3.2 Radio source properties and spectral energy distribution models

In this section, we investigate the physical characteristics of the 27 radio detections, such as sizes, emission measure, electron densities, Lyman-continuum flux, and turnover frequency. These can be estimated from the observational angular sizes and flux densities at a given frequency, assuming the continuum emission comes from a homogeneous, optically thin ionized gas (Urquhart et al. 2013a; Kalcheva et al. 2018; Yang et al. 2021).

The physical properties of young H II regions can be underestimated or overestimated when using the observational parameters from a single frequency. This is the case primarily for two reasons: first, the young H II region may be optically thick at the observing frequency and second, the angular size of the object is dependant on the observing frequency (Yang et al. 2019). Therefore, in order to accurately estimate the physical properties of young H II regions, it is essential to know their radio spectral energy distribution (SED) over a wide frequency range that cover both optically thick and thin regimes.

Using the available multiwavelength data from CORNISH-North 5 GHz (Purcell et al. 2013), CORNISH-South 5 GHz (Irabor et al. 2023), and MAGPIS 5 GHz Becker et al. 1994), we construct radio SEDs for the 27 H II regions. The 1σ sensitivity for CORNISH-North, South, and MAGPIS is 0.35, 0.11, and 0.179 mJy beam^{-1}. In cases where fluxes from different surveys overlap for our radio sources, we prioritize using the 5-GHz flux densities from the CORNISH-North and South surveys due to their greater consistency within the context of this study. We find that 21 of the 27 radio sources are associated with unresolved or compact 5 GHz radio counterparts and are broken down as: five MAGPIS, six CORNISH-North, and 10 CORNISH-South. For the remainder six sources that are not detected at 5 GHz we use the 3σ rms noise from the 5 GHz maps to determine a lower limit for the flux.

Each radio SED model is constructed using the standard uniform electron density model for a bound ionized H II region given by Mezger & Henderson (1967). The integrated flux density at a given frequency v is given by equation (1) using the Rayleigh Jeans approximation:

$$S_v = \frac{2kv^2\Omega T_e(1 - e^{-\tau})}{c^2},\tag{1}$$

where k is the Boltzmann constant, Ω is the solid angle, T_e is the electron temperature, and c is the speed of light. The optical depth τ of free–free radiation can be represented as a function of frequency (Mezger & Henderson 1967; Dyson & Williams 1997):

$$\tau \propto T_e^{-1.35}v^{-2.1}EM,\tag{2}$$

where we assume the electron temperature $T_e = 10^4$ K (Dyson & Williams 1997) and EM is the emission measure. The standard model of a radio SED is therefore expected to have a rising spectrum at low frequencies $S_v \propto v^{+2}$ and a flat spectrum at high frequencies
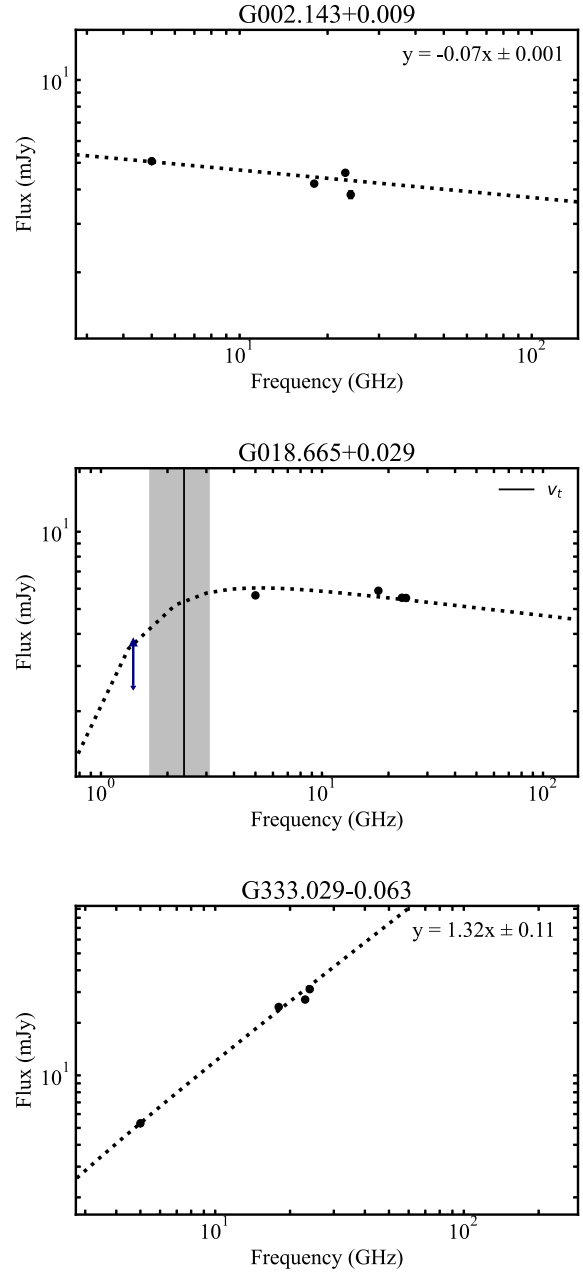

Figure 6. Three examples of radio SED fitting for varying optical depth. Upper panel: SED fitting to the integrated flux density for an optically thin source (G002.143+0.009). Middle panel: SED fitting for radio source G018.665+0.029, an example of a source constrained by both optically thick and thin regimes (Yang et al. 2021). The vertical solid line represents the turnover frequency (v_t) and the shaded region provides an estimation of the uncertainty. The blue triangle represents the 1.4-GHz peak flux density from THOR. Lower panel: SED fitting to the integrated flux density for an optically thick source (G333.029−0.063).

$S_v \propto v^{-0.1}$. Using the model provided by Yang et al. (2021) the radio SED for each source has two free parameters: the electron density (n_e) and the diameter (diam). We obtain the best estimate for the two parameters by fitting the available radio continuum over a range of frequencies. The uncertainties of the integrated flux densities are given as an output from IMFIT (see Table 3) and are taken into consideration during the fitting process. The emission measure can be calculated using the $EM = n_e^2 \times$ diam as demonstrated by
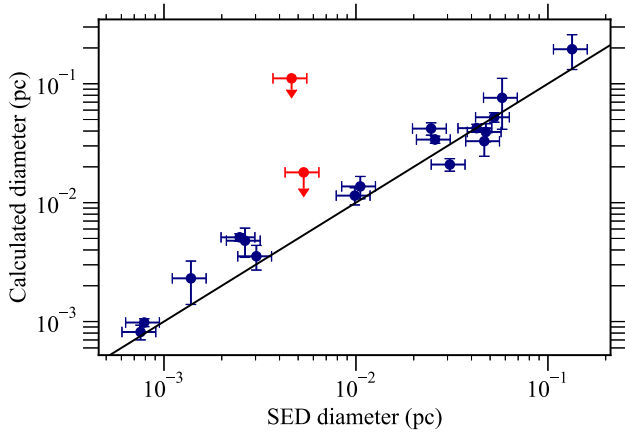
Figure 7. Distribution of the calculated sizes as a function of the SED-derived sizes for the optically thin H II regions in this work. The red upper limits correspond to the two most elongated radio sources in our sample. The black solid line represents the line of equality.

Yang et al. (2021). The model assumes a spherical morphology and represents averaged estimates for the properties (e.g. n_e and diameter) of optically thin ionized gas between 5 and 24 GHz.

In Fig. 6 we present three examples of SEDs with varying optical depths. A complete set of SEDs for the 27 compact sources is provided in Fig. B1 of the appendix, which can be found as online supplementary material. We have identified 11 radio SEDs that lack constraints spanning both optically thick and thin regimes. However, for five of these radio sources located between $l = 12°$ and $18°$, we utilize the peak flux densities from THOR 1.4-GHz (Wang et al. 2018) and MAGPIS 1.4-GHz (White, Becker & Helfand 2005) data to constrain the low-frequency end of the SED and determine the turnover frequency. The additional 1.4-GHz fluxes are presented as upper limits to the peak flux density, as the resolutions of these surveys are significantly larger than the data presented here ($\sim$20 arcsec). The remaining six radio sources that lack constraints across both optically thick and thin regimes have been fitted with a linear function and their sizes have been taken from IMFIT. For these six sources, we use equations (3)–(5) outlined in Section 3.3 to derive the electron density, emission measure, Lyman continuum, and turnover frequencies. Among these six sources, two are optically thin between 5 and 24 GHz, whereas four remain optically thick at 24 GHz. Considering the optically thick nature of these four sources, it is likely that the parameters are underestimated and therefore we present their physical parameters as upper limits to the size and lower limits to the electron density (n_e), emission measure, and Lyman continuum flux ($N_{\rm Ly}$).

3.3 Physical parameters of H II regions

Assuming that the emission of the detected radio continuum originates from homogeneous optically thin H II regions, we have calculated the physical parameters for 27 radio sources using the equations found in Mezger & Henderson (1967) and Rubin (1968). The kinematic distances from the literature are only available for 26 sources therefore our analysis will focus exclusively on these. We compare the results from the 21 optically thin, SED-derived parameters against the output from the equations in Fig. 7. Inspection of this figure reveals two outliers within our sample; these sources correspond to the two most elongated radio sources in our sample and the measured diameters are considered to be upper limits (these are

shown as red upper limits). Excluding these two sources we find the sizes determined from the two methods are in very good agreement.

To check the consistency of the parameters obtained from the SED model and equations we perform a chi-squared test where our null hypothesis states that the equation-calculated parameters are consistent with the values obtained from the SED fitting. Excluding the two elongated sources from the analysis, we find that the diameter, emission measure, and electron density are comparable within the respective uncertainties (p-values >0.7). We utilize the observational parameters extracted from the 24-GHz maps to constrain the physical parameters accurately. The linear diameter of the H II region was calculated using the deconvolved sizes listed in Table 3. We present the fitted SED parameters and derived physical properties in Table 4.

The emission measure (EM) and electron density (n_e) are calculated using Mezger & Henderson (1967) and Rubin (1968):

$$\left(\frac{EM}{\text{cm}^{-6}\,\text{pc}}\right) = 1.7 \times 10^7 \left(\frac{S_\nu}{\text{Jy}}\right) \left(\frac{\nu}{\text{GHz}}\right)^{0.1} \left(\frac{T_e}{10^4\text{K}}\right)^{0.35} \left(\frac{\theta}{\text{arcsec}}\right)^{-2},$$

$$\left(\frac{n_e}{\text{cm}^{-3}}\right) = 2.3 \times 10^6 \left(\frac{S_\nu}{\text{Jy}}\right)^{0.5} \left(\frac{\nu}{\text{GHz}}\right)^{0.05} \left(\frac{T_e}{10^4\text{K}}\right)^{0.175}$$

$$\times \left(\frac{d}{\text{pc}}\right)^{-0.5} \left(\frac{\theta}{\text{arcsec}}\right)^{-1.5}, \quad (3)$$

where ν is 24 GHz, S_ν is the integrated flux density at 24 GHz, T_e is electron temperature, which is assumed to be 10^4K, θ is the angular diameter, and d is the kinematic distance to the source, which has been taken from the literature (i.e. Urquhart et al. 2018, 2022). We do not have an accurate distance for one clump (AGAL002.142+00.009[2]) and so we are unable to calculate reliable measurements for the diameter and emission measure.

In Fig. 8 we show the distribution of the diameter, electron density, and emission measure using the values presented in Table 4. As previously mentioned, upper limits to the diameter and lower limits for the election density and emission measure were determined for the four optically thick sources (i.e. pink regions of the histogram). The vertical dotted line represents the typical criteria of HC H II regions. These plots confirm that our sample have parameter values similar to those of known HC H II regions. The mean values for diameter, electron density, and emission measure are given in Table 5.

3.3.1 Turnover frequency

The behaviour observed in the radio spectrum of an H II region can vary depending on its optical depth, which is frequency-dependant. The frequency for which the optical depth $\tau_\nu = 1$ is known as the turnover frequency (ν_t, Kurtz & Hofner 2005). Using the formula provided by Wilson, Rohlfs & Hüttemeister (2013) assuming a homogeneous, optically thin H II region, the turnover frequency can be expressed as a function of the emission measure and electron temperature T_e.

$$\left(\frac{\nu_t}{\text{GHz}}\right) = 0.3045 \left(\frac{T_e}{10^4\text{K}}\right)^{-0.643} \left(\frac{EM}{\text{cm}^{-6}\,\text{pc}}\right)^{0.476} \quad (4)$$

By considering a typical 20 per cent uncertainty for the diameter and a 20 per cent uncertainty for the emission measure we find that this implies uncertainties of 30 per cent for ν_t (Yang et al. 2021). The top panel of Fig. 9 presents the distribution of the turnover frequency for the 20 H II regions, where their physical parameters were obtained through the SED model. The distribution of our sample peaks at

---

[2]This source is located towards the Galactic centre where kinematic distances are unreliable.

Table 4. Derived physical parameters for 26 H II regions. The sources whose properties were not extracted via the SED fitting are denoted by a †.

Radio name	Diameter (pc)	n_e (10^4 cm^{-3})	EM (10^7 pc cm^{-6})	$\log_{10}[N_{Ly}]$ (photons s^{-1})	ν_t GHz	Spectral type	Classification
G003.438−0.349	0.2649	0.61	0.66	48.62	−	O7	UC H II
G003.910+0.001†	0.0105	9.92	10.37	46.89	5.33	B0.5	HC H II
G004.680+0.277	0.0030	22.97	15.98	45.98	6.55	B1	HC H II
G005.885−0.392	0.0577	8.93	46.03	49.12	10.84	O6	UC H II
G011.904−0.141	0.0134	10.86	5.19	45.67	3.84	B1	HC H II
G012.199−0.034†	0.1749	0.51	0.29	47.90	2.48	O9.5	UC H II
G012.208−0.102†	0.1883	0.92	1.05	48.52	2.19	O7.5	UC H II
G018.461−0.004	0.1903	1.12	2.39	48.82	2.34	O6.5	UC H II
G018.665+0.029†	0.0321	1.72	0.95	46.84	2.38	B0.5	HC H II− UC H II
G018.735−0.227	0.0046	21.77	21.90	46.49	7.61	B0.5	HC H II
G326.475+0.703†	0.0032	7.16	1.82	45.53	−	B1	HC H II
G327.402+0.445	0.0258	5.42	7.59	47.51	4.60	B0	HC H II− UC H II
G331.442−0.187	0.0246	4.68	5.40	47.38	3.91	B0	HC H II− UC H II
G331.542−0.067	0.0308	7.29	16.40	48.03	6.64	O6.5	HC H II− UC H II
G331.557−0.120	0.0525	3.27	5.61	48.01	3.98	O9.5	UC H II
G332.987−0.487	0.0014	118.90	195.35	46.25	−	B0.5	HC H II
G333.029−0.063	0.0026	50.94	68.60	46.47	−	B0.5	HC H II
G333.135−0.432	0.0486	7.81	29.63	48.70	8.79	O7	HC H II− UC H II
G336.983−0.183	0.0099	14.98	22.16	47.17	7.66	B0.5	HC H II
G338.566+0.110	0.0048	19.93	18.87	46.48	7.09	B0.5	HC H II
G338.925+0.556	0.0008	109.97	95.42	46.54	15.34	B0.5	HC H II
G339.282+0.136	0.0025	29.29	21.27	45.99	8.51	B1	HC H II
G339.622−0.121	0.0007	88.01	54.26	45.17	11.73	B1	HC H II
G339.681−1.207	0.0008	53.11	21.30	45.93	7.51	B1	HC H II
G339.884−1.259†	0.0025	17.91	5.31	45.58	−	B1	HC H II
G339.980−0.539	0.0425	4.90	10.21	48.09	5.30	O9	HC H II− UC H II

∼8 GHz and has a mean of ∼9 GHz, which is significantly higher than the expected value of ∼5 GHz for UC H II regions (Kurtz & Hofner 2005).

3.3.2 *Lyman continuum flux*

The number of Lyman continuum photons N_{Ly} per second can be calculated using the integrated flux density and kinematic distance for an optically thin H II region using (Panagia 1973; Carpenter, Snell & Schloerb 1990; Urquhart et al. 2013b)

$$\left(\frac{N_{Ly}}{s^{-1}}\right) = 8.9 \times 10^{40} \left(\frac{S_\nu}{Jy}\right) \left(\frac{d}{pc}\right)^2 \left(\frac{\nu}{GHz}\right)^{0.1} \quad (5)$$

The distribution of the derived N_{Ly} is shown in the lower panel of Fig. 9 and ranges from $10^{44.8}$ to $10^{49.2}$ s^{-1}. Assuming that a single zero-age main-sequence (ZAMS) star is the primary source of the ionizing photons, we estimate the spectral type of the radio detections, which are consistent with ZAMS stars between B2 and O5 (Panagia 1973). The estimated uncertainty in the derived N_{Ly} flux is ∼20 per cent considering the error in the kinematic distance and flux densities (e.g. Sánchez-Monge et al. 2013; Urquhart et al. 2013b). For optically thick compact H II regions, it is likely that the N_{Ly} flux is underestimated; these sources are presented as lower limits (pink region of Fig. 9).

3.4 Distinguishing between HC H II and UC H II regions

In the previous section, we presented the physical parameters for 26 compact H II regions. In Table 6, we summarize the criteria for HC H II and UC H II regions, and the intermediate objects between these stages (e.g. Wood & Churchwell 1989; Kurtz, Churchwell &

Wood 1994; Gaume et al. 1995; Kurtz & Hofner 2005; Hoare et al. 2007; Yang et al. 2021).

In Fig. 10, we show the distribution of the electron density, diameter, and emission measure for the 26 H II regions for which we have accurate distances. The sources that are optically thick in this work are represented as lower limits (arrow pointing upwards) of the electron density and the colours of the data points illustrate the emission measure of each H II region (see the vertical colour bar). On this plot we indicate the region of parameter space we expect to find HC H II regions (i.e. $n_e > 10^5$ cm^{-3} and diam <0.05 pc).

We find that 14 sources satisfy the physical conditions required for HC H II regions; this includes the four optically thick H II regions. A further six sources satisfy the size criterion for HC H II regions but have lower electron densities; these sources are considered to be in a stage between HC H II regions and UC H II regions. The remaining six sources, mainly located in the bottom-right quadrant, are considered to be UC H II regions and contribute ∼20 per cent of our sample.

4 DISCUSSION

4.1 Comparison with known population of compact H II regions

In the preceding section, we have outlined the physical parameters of our sample and identified 14 HC H II regions, six objects that are likely to be in a transition stage between HC H II and UC H II regions, and six UC H II regions. In addition to this, all of the objects in our sample are embedded towards the centres of dense molecular clumps traced by ATLASGAL and are associated with either methanol maser emission or 5-GHz radio emission, all of which are signposts of high-mass star formation. The observed N_{Ly} fluxes support the classification of these objects as ZAMS early B- or late O-type stars.
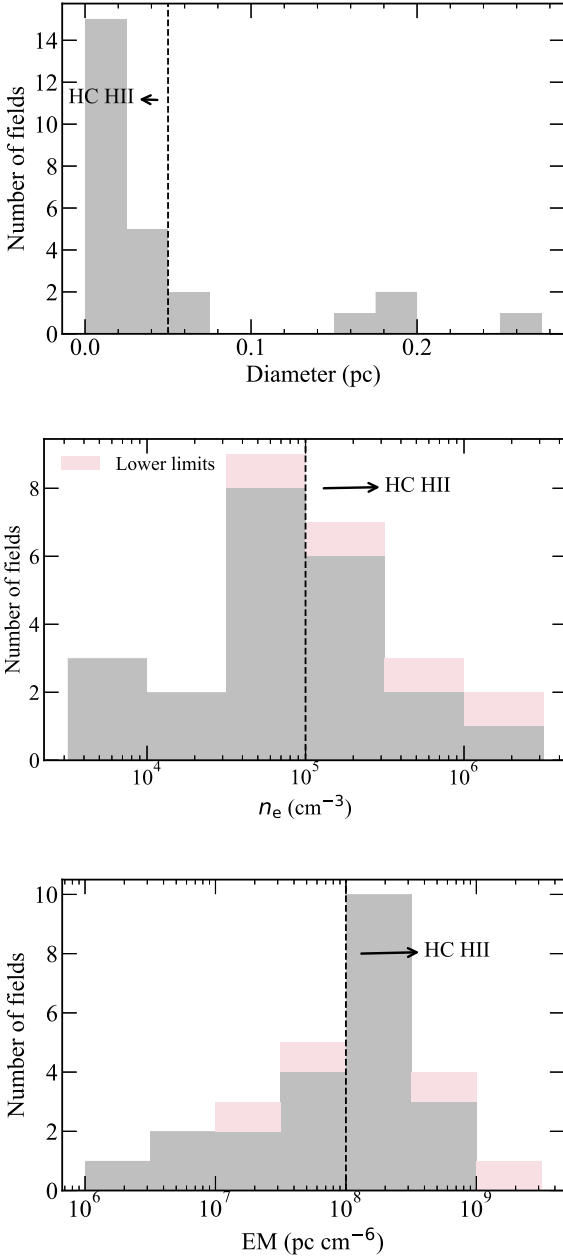
Figure 8. Histograms presenting the diameter (upper panel), electron density (n_e; middle panel), emission measure (lower panel), and the derived physical parameters for the 26 H II regions. The bin sizes are 0.025 pc, 0.5 dex, and 0.5 dex for diameter and n_e and emission measure, respectively. The pink fraction of the distribution represents values that are lower limits. The black arrows emphasize the region of parameter space in which we expect to find HC H II regions.

Table 5. Mean values of the physical parameters for HC H II regions, UC H II regions, and intermediate objects identified in this work.

Parameters	Size (pc)	n_e (cm^{-3})	EM (pc cm^{-6})	ν_t (GHz)
HC H II region	0.007	$10^{5.9}$	$10^{8.7}$	10.4
Intermediate objects	0.03	$10^{5.3}$	10^{8}	7.9
UC H II region	0.15	$10^{4.2}$	$10^{7.9}$	6.2
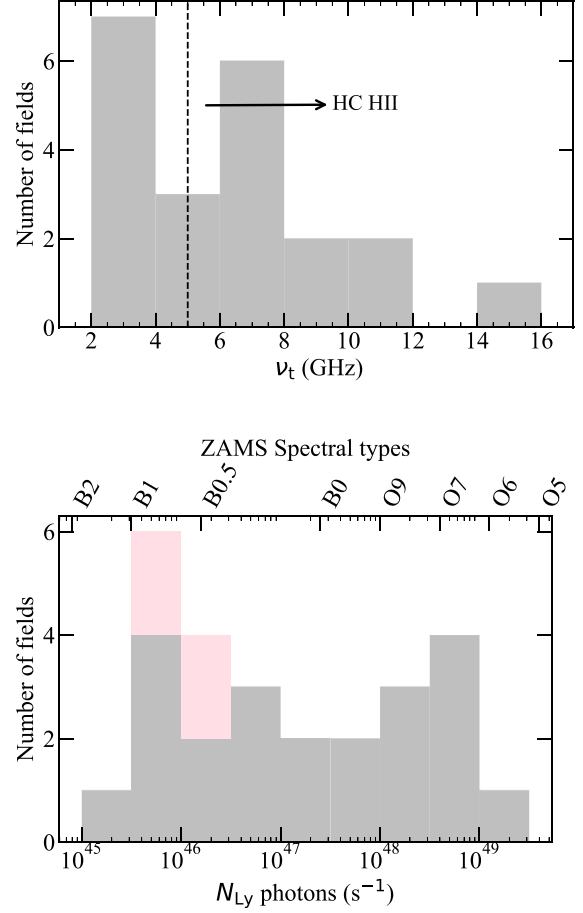
Figure 9. Histograms presenting the turnover frequency (ν_t) and N_{Ly} flux of the derived physical parameters for the 26 H II regions. The bin sizes are 2 GHz and 0.5 dex for ν_t and N_{Ly}, respectively. The pink fraction of the distribution represents values that are lower limits. The black arrow in the upper panel emphasizes the region of parameter space in which we expect to find HC H II regions.

Table 6. Quantitative criteria of the physical parameters for HC H II regions, intermediate objects between the two stages, and UC H II regions from the literature.

Parameters	Size (pc)	n_e (cm^{-3})	EM (pc cm^{-6})
HC H II region	< 0.05	$>10^5$	$>10^8$
Intermediate objects	0.05–0.1	$10^4 - 10^5$	$10^7 - 10^8$
UC H II region	>0.1	$<10^4$	$<10^7$

In this section, we provide a comparison between our sample and the known population of HC H II and UC H II regions.

Many theoretical models such as Mezger & Henderson (1967) and Dyson & Williams (1997) have proposed that H II regions evolve by expanding continuously over time. Their expansion is due to the ionization front moving into the ambient medium faster than the dynamical time of the gas. When the expansion roughly equals the speed of sound $\sim 10\,\mathrm{km\,s^{-1}}$, thermal pressure dominates the flow of the ionized gas, precluding accretion (Spitzer 1978; Dyson & Williams 1980). In this discussion we assume that the star has reached the main sequence and is no longer undergoing accretion, and thus the N_{Ly} flux is constant.
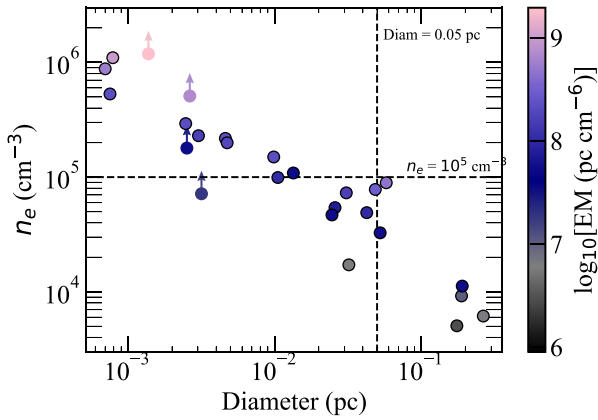
Figure 10. Distribution of the physical properties of the 26 radio sources identified in this work. The colour of the data points represents the emission measure of the radio source. The filled circles with upward-pointing arrows denote upper limits for n_e and emission measure, indicating optically thick radio sources. The vertical and horizontal dotted lines indicate the HC H II region cut-off.

In Fig. 11, we present the distribution of our sample, along with the known HC H II and UC H II regions identified in Yang et al. (2021), as a function of their diameter and electron density. The colours of the

data points correspond to the N_{Ly} flux, as shown in the colour bar. The HC H II, UC H II, and transition objects identified in this work, and the known HC H II and UC H II regions from the literature, are in good agreement with each other, and with the evolutionary models discussed above. The solid black arrow represents the characteristic behaviour of the Strömgren sphere expansion which assumes uniform density and temperature. This illustrates the expected evolutionary trend from HC H II to compact H II regions with the relationship $n_e \propto r^{-1.5}$, where r = diameter/2. Observations have shown that H II regions do not expand spherically due to density inhomogeneities in the surrounding gas, which are likely to impede their expansion. Our sample and the known population of compact H II regions follow the relationship $n_e \propto r^{-1.1 \pm 0.2}$, which, within the uncertainties, provide a better constraint for the expansion of H II regions. This relationship is illustrated by the solid line in Fig. 11.

To further investigate how the individual physical parameters change as a H II region evolves, we present the Lyman continuum output as a function of n_e, diameter, and emission measure for our sample and the known populations of young H II regions in Fig. 12. The optically thick sources are presented as upper limits to the N_{Ly}, n_e, and emission measure. The solid black arrow represents the expected evolutionary trend of the physical characteristics.

In the upper and middle panel of Fig. 12, we present N_{Ly} as a function of diameter and n_e, respectively. The relationship between the diameter and the n_e of the H II region is inversely proportional,
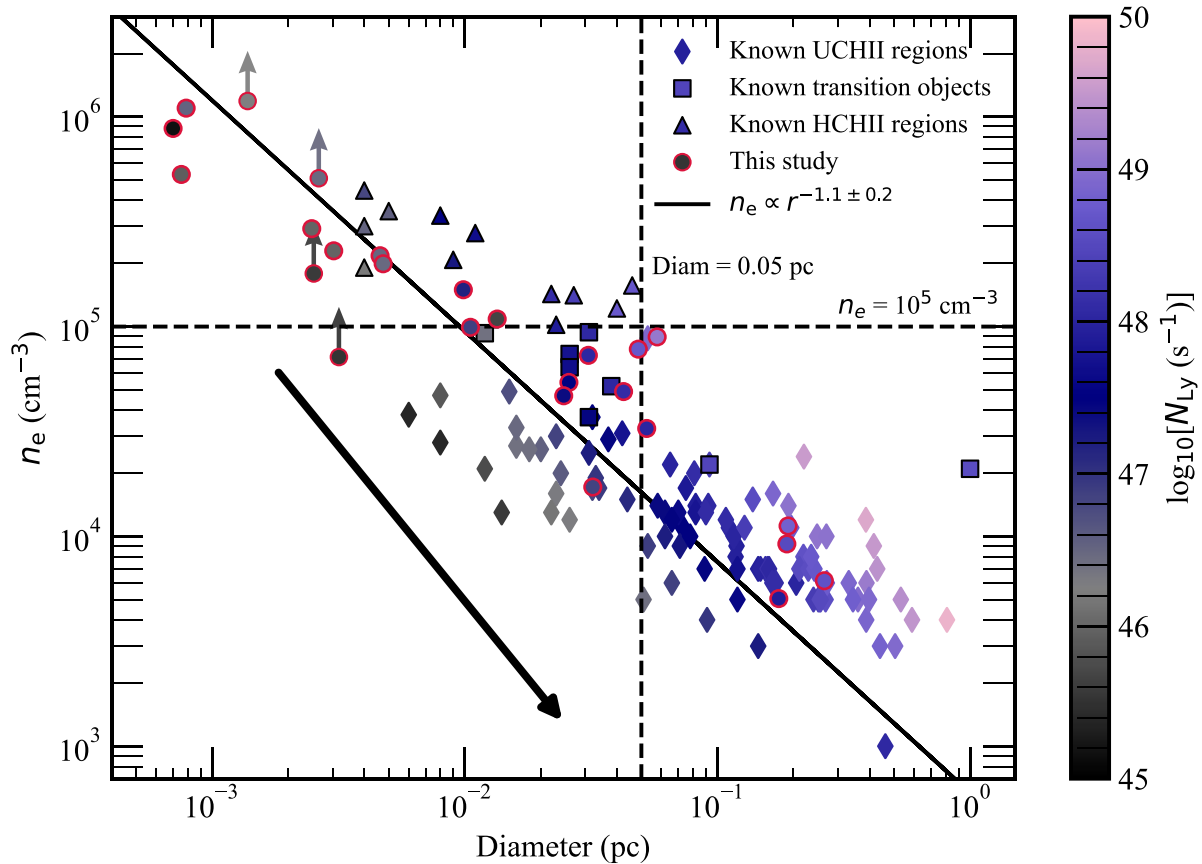
Figure 11. Distribution of the physical properties of the 26 radio sources identified in this work, plus HC H II and UC H II regions identified in Kalcheva et al. (2018), Yang et al. (2019), and Yang et al. (2021). The colour of the data points denotes Lyman-continuum output (N_{Ly}). The diamonds show known UC H II regions and the triangles represent known HC H II regions. The filled circles present the radio sources from this study where we use limits to show the optically thick radio sources. The black solid arrow shows the typical evolutionary trend a HC H II region is likely to follow as these objects expand and the solid black line represents the fitted evolutionary trend of expanding H II regions.
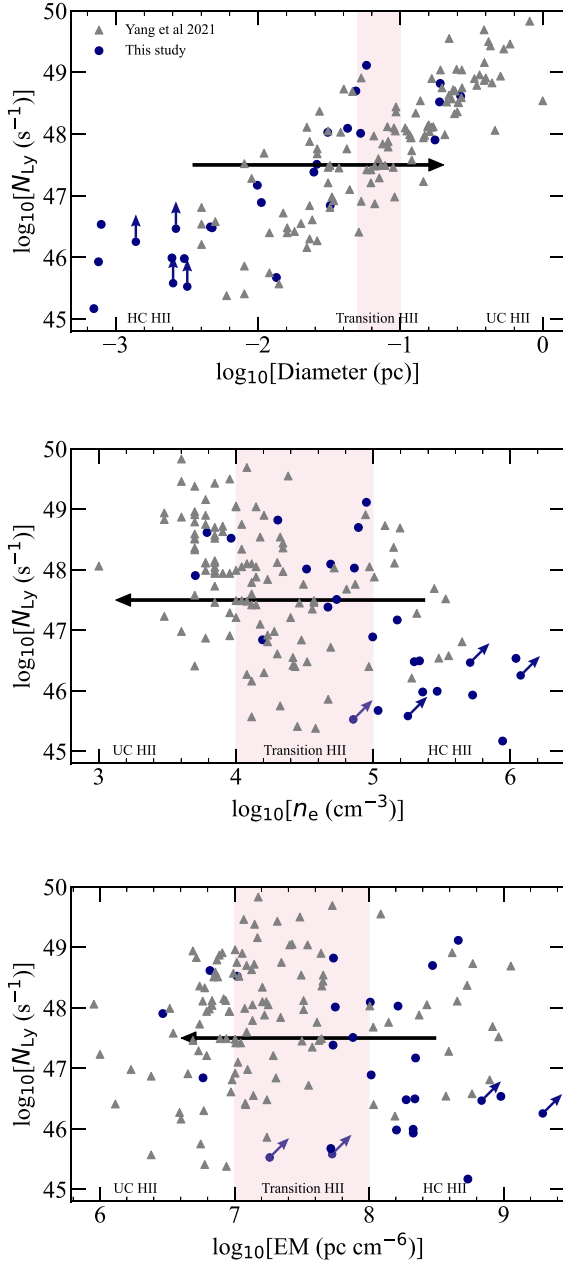
Figure 12. Correlation and evolution of the derived physical parameters. The stages of H II regions are illustrated at the lower section of the plot, with the transition H II regions depicted by the shaded pink region.

indicating that the smallest and densest H II regions are likely to surround early B-type stars. It is interesting to note that the compact HC H II regions (diam $<10^{-2}$ pc) in this work only surround early B-type stars (i.e. $N_{Ly} < 10^{47}\,s^{-1}$), whereas the larger HC H II regions (diam $>10^{-2}$ pc) surround late O-type stars (i.e. with $N_{Ly} > 10^{48}\,s^{-1}$). This could be attributed to the rapid expansion of H II regions around late O-type stars, driven by their high luminosity and strong ionizing photon flux that results in these types of high-mass stars being associated with lower gas density at larger radii. Additionally, there is a region of parameter space (see the lower right corner of the upper panel and the lower left corner of the middle panel in Fig. 12) where we do not find any UC H II regions that surround early B-type stars. This is likely due to either sensitivity as

the surface brightness decreases as they expand or due to the nature of the interferometric observations that filter out sources above a certain angular scale.

In the lower panel of Fig. 12, we present the distribution of the N_{Ly} flux with respect to the emission measure. We find no correlation between the N_{Ly} flux and the emission measure of evolving H II regions, suggesting that the emission measure is invariant with respect to N_{Ly}. A similar trend has been reported in the works of Yang et al. (2021), who confirm that there is effectively no relationship between N_{Ly} and emission measure (e.g. see section 5.1 from Yang et al. 2021).

The HC H II regions detected in this study exhibit a distinctive characteristic whereby they tend to be associated with lower bolometric-luminosity stars. In Fig. 13, we show cumulative distribution functions for the bolometric luminosity and N_{Ly} flux for the HC H II regions identified in the literature and the HC H II regions confirmed in this work. Upon initial inspection, the distributions appear to be different. The grey dotted line in Fig. 13 represents the median of our sample, and the navy dotted line indicates the median value of Yang et al. (2021) sample. It appears that the majority of our sample tends to surround early B-type stars, whereas the HC H II from the Yang et al. (2021) sample surrounds late O-type stars. The difference in median values confirms there is a substantial distinction between the two HC H II region samples. To determine if there are similarities in the bolometric luminosities and Lyman fluxes between the two samples of HC H II regions, we use a two-sample Kolmogorov–Smirnov (KS) test. Our null hypothesis states that the two samples of HC H II regions are drawn from the same underlying distribution; this can be rejected if the p-value is lower than 3σ (i.e. <0.0013). We find that the distribution of the Lyman continuum flux is significantly different, while the bolometric luminosity shows a marginal difference of $\sim2.8\sigma$.

In Fig. 14 we show the Lyman photon flux as a function of bolometric luminosity for both samples of HC H II regions. The distribution further confirms that the HC H II regions identified in this work surround lower luminosity stars. A possible explanation for this could be that the HC H II regions reported in previous literature were identified from a lower frequency survey that is sensitive primarily to the brightest HC H II regions, due to the fact that they are optically thick at these frequencies, whereas our sample of HC H II regions is targeted towards sites of methanol masers that are not intrinsically bright at higher resolutions. In addition, high-frequency radio observations are more sensitive to lower luminosity high-mass stars.

None the less, as demonstrated by Fig. 14, the H II regions within our sample align well with the broader population of H II regions. All of the objects are located significantly above the jet line (see dot–dashed line on Fig. 14), apart from G339.884, which will be discussed later. This alignment provides strong evidence of their association with massive stars and rules out the possibility of them being radio jets, which tend to have lower radio luminosities compared to their bolometric luminosity.

4.2 Physical properties of the optically thick H II regions

We have identified four HC H II regions that remain optically thick ($\alpha > 0.5$) and compact (diam <0.05 pc) at 24 GHz. These are likely to be the youngest H II regions in our sample. The radio sources are all within 1 arcsec of the methanol-maser position. Given the 1-arcsec positional uncertainty in the maser positions (Green et al. 2010), we consider them coincident for this discussion. Considering that methanol masers often reside in the dusty molecular envelope
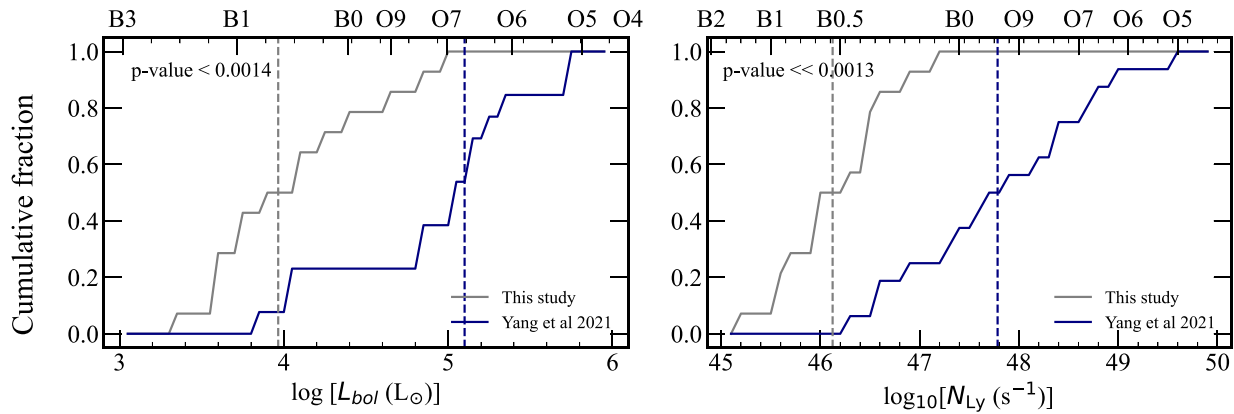
Figure 13. Cumulative distribution functions for bolometric luminosity (left panel) and N_{Ly} flux (right panel) for the sample of HC HII regions identified in this work and in the literature (Yang et al. 2021). The dotted line represents the median value of each sample.
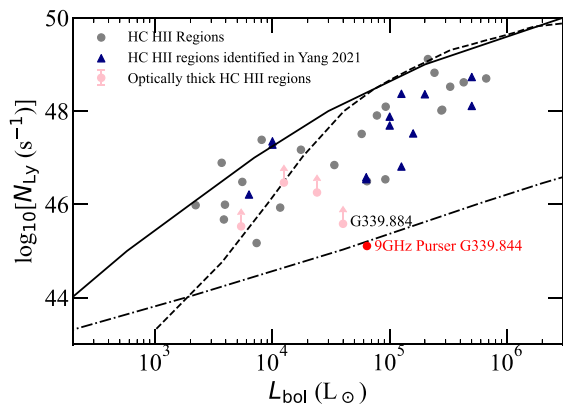

Figure 14. Lyman-continuum photon flux as a function of bolometric luminosity for the HC HII regions identified in this work and in the literature. The grey and pink circles show our sample of HC HII and optically thick HC HII regions, respectively. The blue triangles represent the HC HII and transition objects identified in Yang et al. (2021). The dashed line indicates the relationship for OB ZAMS-star models (Martins, Schaerer & Hillier 2005; Davies et al. 2011) and the dot–dashed line represents a fit to radio jets found in Purser et al. (2016, 2021). The solid black line corresponds to the Lyman continuum expected from a blackbody with the same radius and temperature as a ZAMS star (see Sánchez-Monge et al. 2013 for more detail).

(Urquhart et al. 2015), they are sensitive probes for discovering the earliest stages of massive star formation (Breen et al. 2011). Methanol masers are pumped by infrared radiation and require high temperatures and densities to be stimulated (Sobolev & Deguchi 1994). These conditions are likely to be found between 100 and 1000 au from the high-mass protostellar object and are signposts of ongoing disc accretion (Breen et al. 2013).

Other molecular masers (i.e. H_2O and OH) can provide valuable insights into the environment, kinematics, and feedback processes associated with massive star formation. Water masers are collisionally pumped and the conditions required to excite them are high densities ($\sim 10^7$ cm^{-3}) and temperatures up to 500 K (Elitzur, Hollenbach & McKee 1992). These conditions are exclusively found in the shocked gas associated with molecular outflows (Claussen 2002). Hydroxyl (OH) masers are also collisionally pumped and are widely recognized to trace shocked gas in the interface between neutral hydrogen and molecular hydrogen known as photodissociation regions (Frail & Mitchell 1998). OH masers

are thought to trace a slightly more evolved evolutionary stage than the class II CH_3OH masers (Beuther et al. 2019).

In the following section, we combine our findings with results from the literature to build a more comprehensive picture of the environments in which these sources are embedded. Detailed characteristics of the clump are provided in Table 7 and images of their infrared environment are shown in Figs 15–18. Given that these are optically thick, the N_{Ly} photon flux and the derived ZAMS spectral type for these sources are lower limits.

G326.475+0.703 (Fig. 15): The high-frequency radio emission is embedded towards the centre of the dense molecular clump AGAL326.474+00.702 (Urquhart et al. 2014b), which is itself associated with the RCW 95 massive star-forming region (Rodgers, Campbell & Whiteoak 1960). This particular clump has been classified as an infrared dark cloud (i.e. SDC G326.476+0.706; Peretto & Fuller 2009) and has a mass of 840 M$_\odot$ and volume density of 10^6 cm^{-3} (Urquhart et al. 2014b). Inspection of the IRAC mid-infrared images reveals the presence of a bright source to the south-east but this is located on the periphery of the central part of the clump, which is mid-infrared quiet at 8 and 24 μm.

High-resolution (~ 4-arcsec) observations of the dust emission at 350 GHz ($\lambda \sim 0.9$ mm) by Csengeri et al. (2017a) reveal the presence of three dense cores ($\sim 10^7$ cm^{-3}) located towards the centre of the clump. These are classified as 326.4745+0.7027-MM1, MM2, and MM3, with masses of 150 M$_\odot$, 27 M$_\odot$, and 20 M$_\odot$, respectively. The HC HII region and the methanol maser are both positionally coincident with the centre of the most massive core MM1, which is itself located at the centre of the clump. At a distance of 2.6 kpc, the angular separation between the HC HII region, methanol maser, and the centre of the core put them within approximately 1550 au of each other, roughly corresponding to the size of a typical high-mass protostellar accretion disc taking into account the uncertainties in the positions.

Analysis by Cyganowski et al. (2008) has revealed the presence of two extended green objects (EGOs) that are located to the east and west of the central core. The positions of these are shown in Fig. 15 as red crosses. EGOs are identified by an excess in the 4.5-μm IRAC band and is thought to be the result of strong emission from the rotationally excited H_2 ($v = 0 - 0$) and CO ($v = 1 - 0$) band-head emission (cf. fig. 1 of Reach et al. 2006) that fall within this waveband. The excited H_2 results from shocked gas associated with outflows, while the CO bandhead emission at 2.3 μm is thought to trace warm ($T = 2500-5000$ K) and dense ($\sim 10^{11}$ cm^{-3}) gas (Chandler, Scoville & Carlstrom 1993) and is

Table 7. Physical characteristics of the optically thick sources and their embedding environments. The typical error in the ATLASGAL clump properties is estimated to be of the order of 20 per cent.

Radio name	CSC name	ATLASGAL clump properties				Radio-derived properties				
		Distance (kpc)	Mass ($10^2\,M_\odot$)	Luminosity ($10^5\,L_{bol}$)	Temperature (K)	Diameter (10^{-3} pc)	n_e ($10^4\,cm^{-3}$)	EM (10^7 pc cm^{-6})	$\log_{10}[N_{Ly}]$ (s^{-1})	ZAMS Spectral type
G326.475+0.703	AGAL326.474+00.702	2.6	8.4	5.4	20.7	3.2	7.2	1.8	45.5	B1
G332.987−0.487	AGAL332.986−00.489	3.5	40[a]	24[c]	24.6[a]	1.4	118.9	195.3	46.3	B0.5
G333.029−0.063	AGAL333.029−00.061	2.8	2.5	12.5	30.8	2.6	50.9	68.6	46.5	B0.5
G339.884−1.259	AGAL339.884−01.257	2.1	4[b]	40[d]	–	2.5	17.9	5.3	45.5	B1

Note. references. [a]He et al. (2016), [b]Liu et al. (2019), [c]Wheelwright et al. (2012), [d]Zhang et al. (2019).

thought to be associated with accretion discs. Given that these two EGOs appear approximately 8 to 10 arcsec away from the central core and outside of the lowest contour of the ALMA map suggests that the excess emission could be due to the presence of a bipolar molecular outflow rather than accretion. However, analysis of the ALMA CO (3-2) data from SPARKS does not reveal an outflow in the direction of the northern EGO (EGO G326.47+0.70) and so the true nature of the emission is less certain. A detailed analysis of these data will be described in a future publication.

Although there is no significant 8- or 24-µm emission, there is strong 70-µm emission seen in the HiGAL image (Molinari et al. 2010), resulting in this source being classified as protostellar in Urquhart et al. (2022). The association of the EGOs and presence of a methanol maser strongly suggests that a high-mass protostar is forming within the core and that active accretion is ongoing. Furthermore, the presence of the radio emission would further indicate that the high-mass protostellar object has recently arrived on the main sequence and began ionizing its natal environment. The Lyman flux and bolometric luminosity are consistent with the presence of a high-mass ZAMS star with a spectral type of B1 or earlier, corresponding to a stellar mass of more than $10\,M_\odot$.

G332.987−0.487 (Fig. 16): This object is compact, with an angular size similar to that of the beam (~0.4 arcsec) and is embedded towards the centre of the dense molecular clump (AGAL332.986−00.489; Contreras et al. 2013). This clump is embedded within the G333 giant molecular cloud, which is located at a distance of 3.6 kpc (Lockman 1979) and is itself the fourth most active star-forming region in the Galaxy (Urquhart et al. 2014a). Observations by Billington et al. (2019) using NH_3 (1,1) and (2,2) have identified a high-density region towards the centre of the ATLASGAL clump that has an approximate size of 0.2 pc. The radio emission is coincident with the centre of both NH_3 and ATLASGAL clumps and the methanol maser G332.987−00.487 (Caswell 2010) which is offset by 0.7 arcsec east of the radio emission.

The mid-infrared environment reveals the presence of a bright 8-µm point source associated with an EGO (i.e. extended 4.5-µm emission), which is slightly offset from the peak of the dust emission. This has been classified as a MYSO in the RMS survey by Lumsden et al. (2013) and more recently by ATLASGAL in Urquhart et al. (2022). High-resolution near-infrared spectroscopy of the CO ($v = 2 - 0$) bandhead emission towards a sample of MYSOs that includes this source was conducted by Ilee et al. (2013) using the Very Large Telescope. CO bandhead emission at 2.3 µm traces warm ($T = 2500-5000\,K$) and dense ($\sim 10^{11}\,cm^{-3}$) gas. These conditions are consistent with the environment typically found in the inner regions of accretion discs (Wheelwright et al. 2012; Ilee et al. 2013). The presence of the CO bandhead and MMB methanol maser indicates ongoing accretion through a disc surrounding the MYSO. Ilee et al. (2013) assumed a geometrically thin disc and used a model to determine the disc properties surrounding the associated MYSO. An analytical model of the temperature and density was used to fit the individual line profiles between 2.296 and 2.298 μm. The mass and effective temperature determined by Ilee et al. (2013) for MYSO G332.9868−00.4871 is $16.6\,M_\odot$ and 30 000 K, respectively. These values are consistent with the MYSO having a ZAMS spectral type of B0.5, which is also consistent with the ionizing photon flux derived from the radio data.

The angular offset between the HC H II region and MYSO G332.9868−00.4871, which is associated with the accretion disc, is ~0.3 arcsec, and given the positional uncertainties these are considered to be associated with the same object.
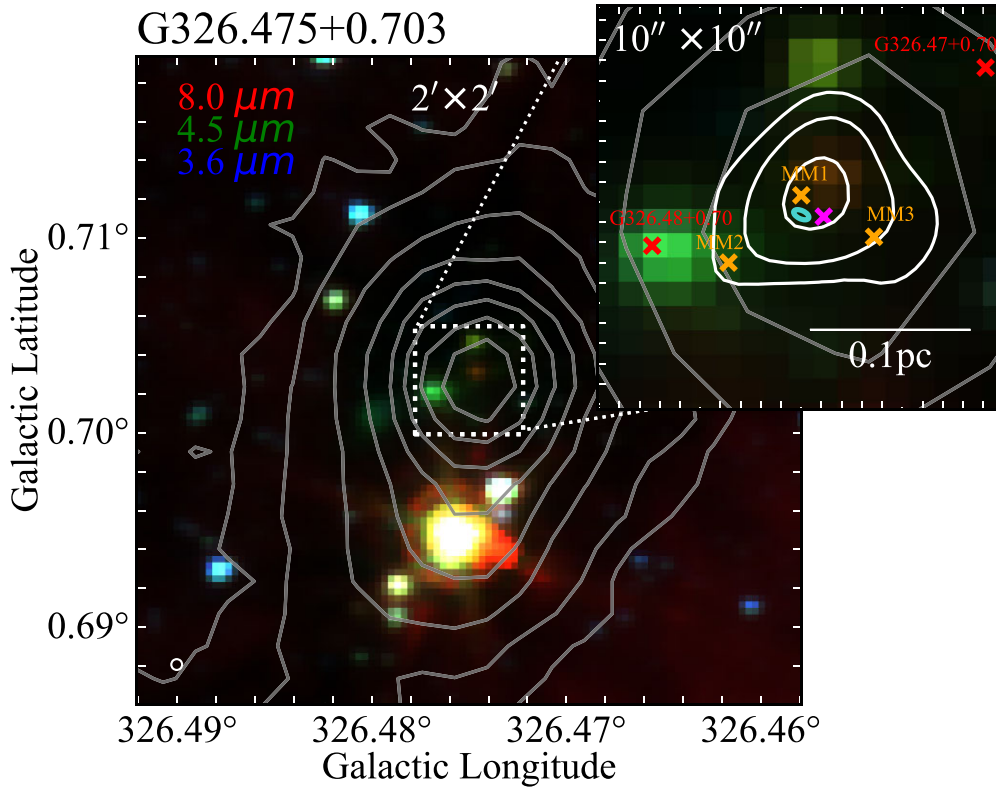
Figure 15. Three-colour composite images from *Spitzer* GLIMPSE 8-μm (red), 4.5-μm (green), and 3.6-μm (blue) bands for HC H II region G326.475+0.703. In the upper right zoomed panel, the cyan ellipse shows the high-frequency (24-GHz) radio source and the magenta crosses show the position of the MMB methanol maser. The 870-μm dust emission from ATLASGAL is traced by the grey contours. The white contours show the 350-GHz dust continuum emission from SPARKS where the orange crosses present the positions of the dense cores as identified in Csengeri et al. (2017a). The red cross shows the peak position of EGOs as identified in Cyganowski et al. (2008).

G333.029−0.063 (Fig. 17): This very compact source is located towards the centre of dense molecular clump AGAL333.029−00.061 (Contreras et al. 2013), which is also embedded within the G333 giant molecular cloud (Lockman 1979). The mid-infrared environment reveals multiple point sources, indicating the presence of a small protocluster located within the central part of the clump, but offset from the peak of the dust emission, which is mid-infrared dark. The high-frequency radio emission is coincident with the edge of the brightest of the mid-infrared sources, which is extended and located to the south of the centre of the clump. High-resolution (∼2.5-arcsec) continuum maps at 5 GHz produced by CORNISH-south (Irabor et al. 2023) reveal the presence of an unresolved point source, G333.0290−0.0631, that is offset by 0.5 arcsec from the high-resolution source; however, the resolution of the CORNISH observations is a few arcsec and given the uncertainties, the radio emission is likely to be associated with the same star. The extended nature of the 8-μm emission and its association with the 5-GHz radio continuum emission has led to this source being classified as an H II region in the RMS survey (Lumsden et al. 2013).

Methanol, H_2O, and OH maser species have been detected within 3 arcsec of the HC H II region. The H_2O maser is located north-east of the methanol maser, which is coincident with the 5-GHz radio continuum emission (offset ∼0.3 arcsec). Two 1720-MHz OH masers have been recently identified towards this region by Qiao et al. (2020) as part of the Southern Parkes Large-Area Survey in Hydroxyl (SPLASH) project (Dawson et al. 2014). These are identified as G333.029−0.063-1665A and G333.029−0.063-1720A and are shown as blue crosses in Fig. 17. The tight correlation in

position between maser species strongly suggests that the high-mass protostellar object is still undergoing accretion. The presence of the H_2O maser confirms that there is shocked gas, which is likely to originate from outflows. Furthermore, considering 1720-MHz OH masers trace shocked gas towards the edge of an expanding H II region bubble, it is likely that the embedded high-mass protostar has recently begun ionizing its surroundings.

G339.884−1.259 (Fig. 18): The high-frequency radio emission is detected towards the centre of dense molecular clump AGAL339.884−01.257 (Contreras et al. 2013) and is located at a distance of 2.1 ± 0.4 kpc (Krishnan et al. 2015). High-resolution (∼0.06-arcsec) images made with the mid-infrared spectrometer OSCIR at the Keck Observatory have resolved the mid-infrared emission into three distinct peaks (De Buizer et al. 2002); these are identified as 1A, 1B, and 1C, all of which lie within a region of ∼3000 au. High-resolution (∼0.3-arcsec) ALMA submillimetre observations of dust emission at 220 GHz (1.3 mm) by Zhang et al. (2019) reveal the presence of a dense core that has a gas mass between 58 and $23\,M_\odot$ assuming a temperature range of $30-70$ K, respectively. The HC H II region and the methanol maser are both positionally coincident with the centre of the core, which is itself located towards the centre of the ATLASGAL clump. It is interesting to note that the submm peak does not coincide with any of the mid-infrared peaks. Instead, it appears to be situated in the gap between mid-infrared points B and C, and is therefore mid-infrared quiet at 10 and 18 μm (De Buizer et al. 2002).

Molecular masers such as H_2O and OH have been detected within the centre of the core. Two 1720-MHz OH masers are positioned
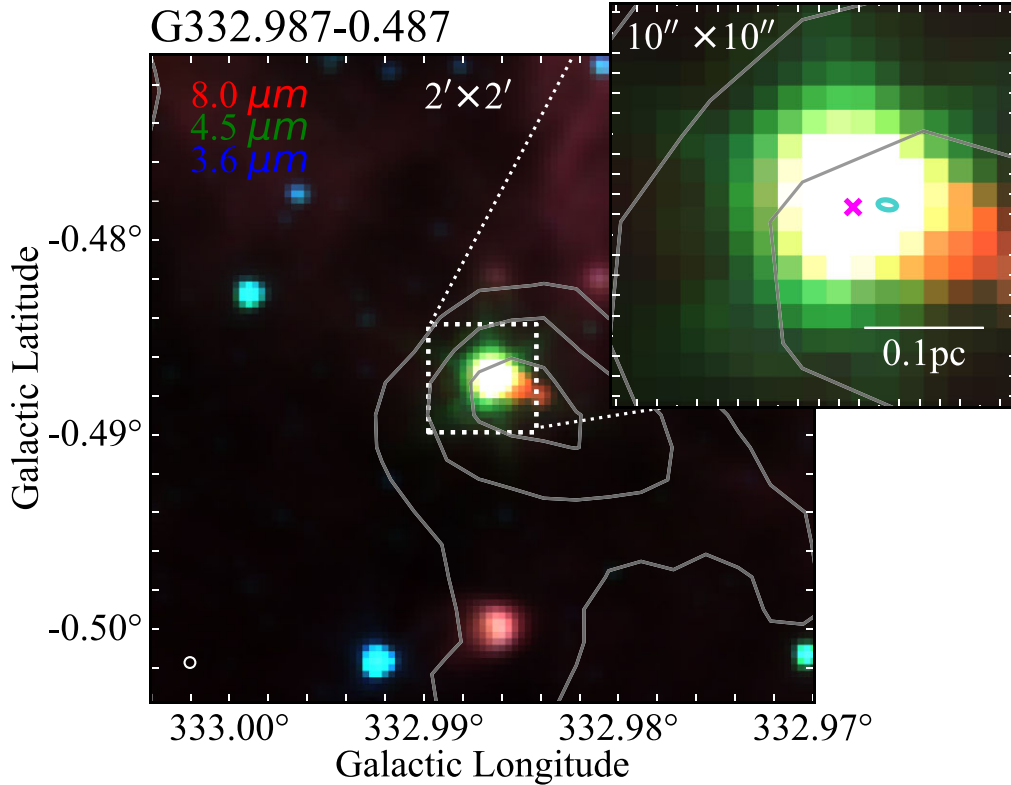
Figure 16. Three-colour composite images from *Spitzer* GLIMPSE 8-µm (red), 4.5-µm (green), and 3.6-µm (blue) bands for HC H II region G332.987−0.487. The 870-µm dust emission from ATLASGAL is traced by the grey contours. In the upper right zoomed panel, the cyan ellipse shows the high-frequency (24-GHz) radio source and the magenta cross shows the position of the MMB methanol maser.

to the south-west of the radio emission and are offset by ∼1 arcsec (Caswell et al. 1995). A H$_2$O maser is located 0.7 arcsec east of the radio source. As previously mentioned, these masers are known to trace the shocked gas within an outflow cavity. The ALMA ^{12}CO(2−1) observations by Zhang et al. (2019) reveal a large-scale molecular outflow with a northeast–southwest orientation emanating from the centre of the submm emission. These are shown as solid arrows in Fig. 18. A secondary, weaker outflow (dotted arrows on Fig. 18) has been identified in a southeast–northwest orientation, which roughly coincides with an ionized radio jet identified by Purser et al. (2016) (indicated by green arrows on Fig. 18). The orientation of these outflows would strongly suggest the presence of an embedded proto-binary system with individual outflows roughly perpendicular to each other (Zhang et al. 2019).

Comparing our high-frequency flux densities with those reported in the literature, we find that the fluxes recorded in this study are approximately double the values reported in Purser et al. (2016). We verified our calibration and the fluxes derived for the primary flux calibrator and find it to be consistent with expected values within 10 per cent. Since the observations by Purser et al. (2016) were taken in 2011 February, the differing flux densities could be attributed to the variability of the radio sources, considering the time between the observation sets. The variability of flux densities has been reported in several compact and young H II regions detected by the GLOSTAR survey (e.g. Yang et al. 2023). At a distance of 2.7 kpc and a bolometric luminosity of $6.4 \times 10^4 \, \mathrm{L_\odot}$, Purser et al. (2016) use the 9-GHz radio flux to derive the radio luminosity. They find that the object aligns well with the expected luminosity of a radio jet. However, considering the object is optically thick at 9 GHz

it is likely that the radio luminosity is underestimated. As shown in Fig. 14, our 24 GHz radio flux puts this source above the expected radio jet line. Our observations give us a better constraint on the lower limit; however, the true nature of this object is still uncertain.

4.3 Matches with ALMA cores

The search for high-mass protostars with ALMA up to 5 kpc (SPARKS) project observed 46 mid-infrared quiet ATLASGAL clumps with ALMA in an effort to characterize objects in the earliest stages of high-mass star formation (Csengeri et al. 2017a). Given that methanol masers are considered to be associated with the earliest stages in high-mass star formation, many of the cores identified by SPARKS host methanol masers: 42 out of the 112 cores (37.5 per cent; Chibueze et al. 2017). Comparing the SPARKS cores with our sample of high-frequency compact radio sources, we find four matches located in three SPARKS fields. One of these (G326.475+0.703) has already been discussed in the previous subsection, the other two radio sources are G338.925+0.556 and G339.681−1.207, which are matched with SPARKS fields G338.9249+0.5539 and G339.6802−1.2090, respectively. Next, we provide a summary of the other two matches between SPARKS cores and radio sources.

G338.925+0.556 (Fig. 19): There are three SPARKS cores associated with the ATLASGAL clump AGAL338.926+00.554. The most massive core (∼250 M$_\odot$, MM1) is located towards the centre of the clump and is mid-infrared quiet. The second most massive core (∼200 M$_\odot$, MM2) is located to the north-east of MM1, and it is this core that is coincident with a methanol (G338.925+00.557; Caswell 2009), OH maser (OH 338.925+00.557; Sevenster et al.
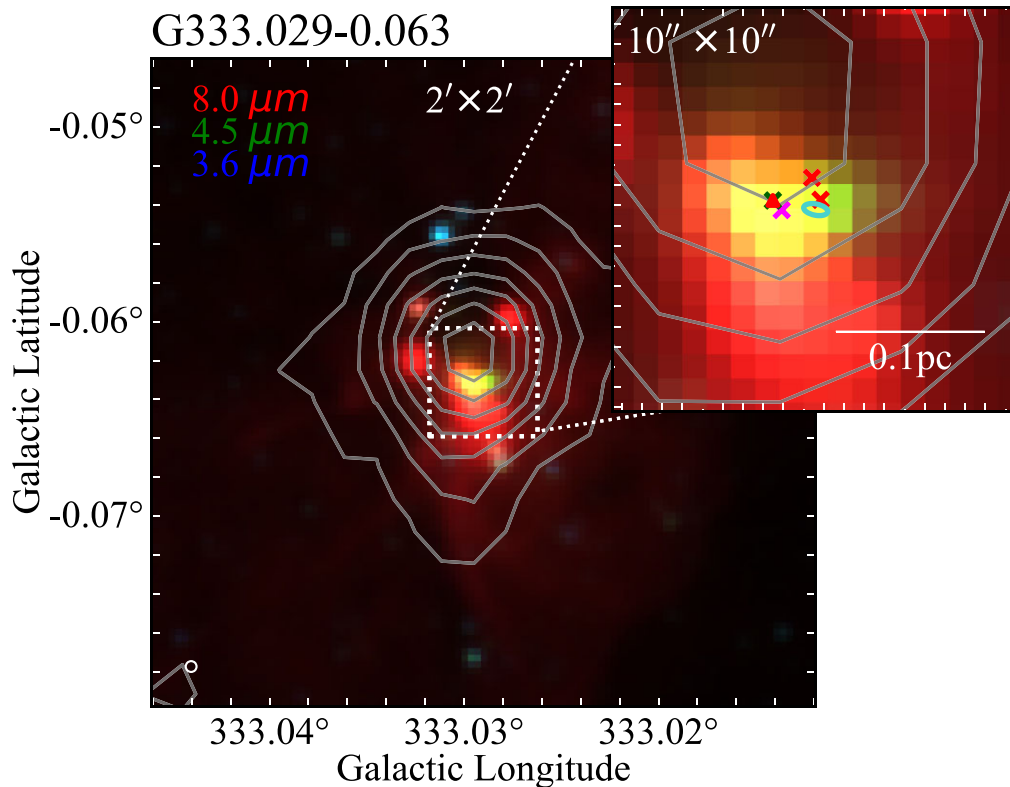
Figure 17. Three-colour composite images from *Spitzer* GLIMPSE 8-µm (red), 4.5-µm (green), and 3.6-µm (blue) bands for HC H II region G333.029−0.063. The 870-µm dust emission from ATLASGAL is traced by the grey contours (Schuller et al. 2009). In the upper right zoomed panel, the cyan ellipse shows the high-frequency (24-GHz) radio source and the magenta cross shows the position of the MMB methanol maser. The 5-GHz CORNISH-South radio source is shown as a red triangle (Irabor et al. 2023). OH and H_2O masers are shown as red and green crosses, respectively. (Breen & Ellingsen 2011; Qiao et al. 2020).

1997), and compact high-frequency (24 GHz) radio source identified in this work (G338.925+0.556). It is also associated with a compact infrared source that appears to have an excess 4.6 µm emission, consistent with the presence of shocked gas. The angular offset for the radio, excess 4.6 µm emission, and methanol maser and MM2 are all less than 1 arcsec, which at the distance of 4.2 kpc (Urquhart et al. 2022) corresponds to a physical offset of less than 0.02 pc and so can be considered to be associated with each other. The third SPARKS core (∼60 $M_\odot$, MM3) is coincident with an EGO (EGO G338.92+0.55(a); Cyganowski et al. 2008) indicating star formation in this core is already underway.

The high-frequency radio source is not detected by CORNISH-South at 5 GHz (Irabor et al. 2023) and is also a non-detection at 8.6 GHz (Urquhart et al. 2007a). Using the 3σ of these radio maps as upper limits we have fitted the radio SED and this shows the H II region is likely to be optically thick at 5 GHz with a turnover close to 18 GHz, consistent with this being classified as a HC H II region. The Lyman flux is 3.4×10^{46} photons s^{-1} consistent with being ionized by ZAMS star with a spectral type of B0.5.

To the north of the SPARKS cores (MM3), but still located within the boundary of the ATLASGAL clump, is a low surface brightness compact H II region (G338.9237+00.5618) and there is a high-mass YSO (G338.9196+00.5495) located to the south-west of the SPARKS cores; both the H II region and YSO have been identified by the RMS survey (Lumsden et al. 2013). The high-mass YSO is associated with an OH maser (OH 338.92+00.55; Caswell et al. 1995) and EGO (EGO G338.92+0.55(b); Cyganowski et al. 2008). The mid-infrared composite image also reveals the presence of several other compact infrared sources coincident with the clump.

With a mass of ∼9500 $M_\odot$ (Urquhart et al. 2018) this clump is one of the most massive in the ATLASGAL catalogue. The bolometric luminosity of the clump is 1.4×10^5 $L_\odot$, which is sufficient to indicate the presence of a single star of spectral type O6 or a cluster consisting of several high-mass stars where the most massive is of spectral type O7. The presence of multiple high-mass cores and embedded infrared sources including a compact H II region, a high-mass YSO, and newly identified HC H II region as well as being associated with numerous EGOs and methanol and OH masers make it clear this clump is hosting a young protocluster.

G339.681−1.207 (Fig. 20): The radio source G339.681−1.207 is embedded in the ATLASGAL clump AGAL339.681−01.209, which is located at a distance of 2.4 kpc and has a mass and bolometric luminosity of ∼600 $M_\odot$ and 1200 $L_\odot$, respectively (Urquhart et al. 2022). The SPARKS data reveal the presence of three cores located towards the centre of the clump; these are labelled as MM1, MM2, and MM3 and have masses of 46, 24, and 21 $M_\odot$, respectively.[3] MM1 and MM2 are located towards the centre of the clump (∼2 arcsec) and MM3 is slightly offset from the centre of the clump (∼7 arcsec).

The most massive core appears to be relatively quiescent with no known masers or EGO associations. The compact high-frequency radio source is coincident with the lowest mass core (MM3) being located ∼2.4 arcsec from the centre of the core, corresponding to a physical offset of 0.03 pc. The Lyman flux

---

[3]These masses have been rescaled using a distance of 2.4 kpc and so differ from the values given in Csengeri et al. (2017a), which were determined using a distance of 1.8 kpc.
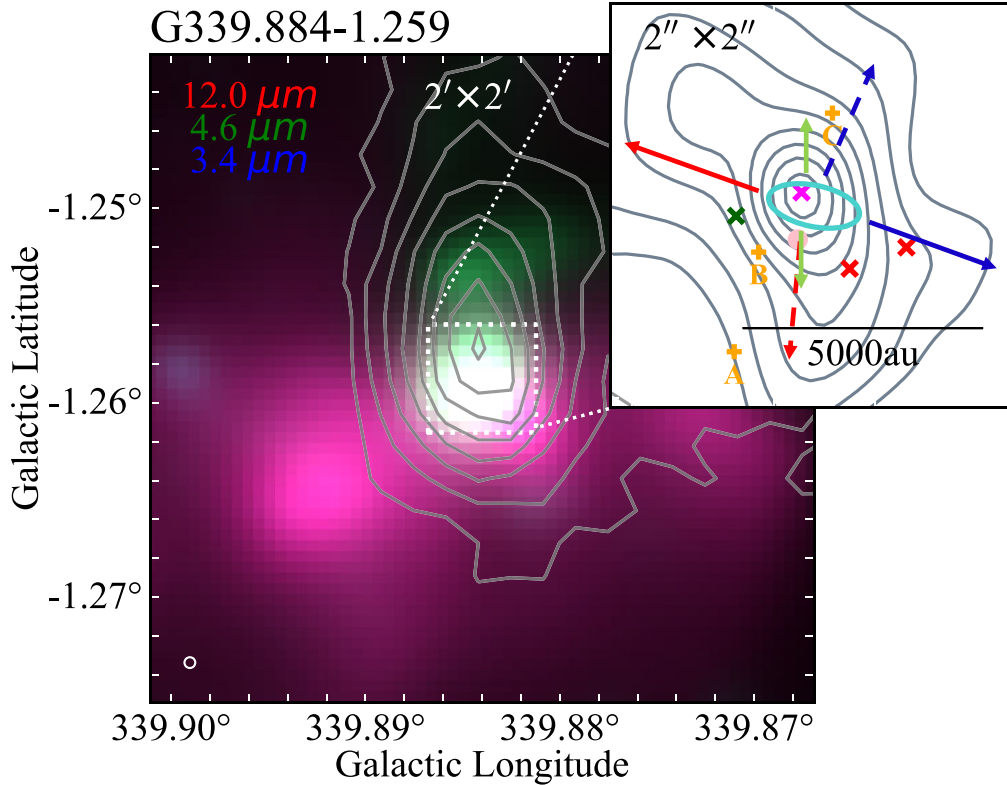
Figure 18. Three-colour composite images from WISE 12-μm (red), 4.6-μm (green), and 3.4-μm (blue) bands for HC H II region G339.884−1.25. The 870-μm dust emission from ATLASGAL is traced by the grey contours. In the upper right zoomed panel, the cyan ellipse shows the position of the high-frequency (24-GHz) radio source and the magenta cross shows the position of the MMB methanol maser. OH and H_2O masers are shown as red and dark green crosses, respectively (Breen & Ellingsen 2011; Qiao et al. 2020). The 10-μm peak positions are shown as orange plus symbols. The SPARKS 1.3-mm continuum emission is traced by the dark grey contours. The dot and dashed arrows show red-shifted and blue-shifted CO outflows reported in Zhang et al. (2019). The lime green arrows represent the ionized jet as identified in Purser et al. (2016).

for G339.681−1.207 is 9.3×10^{44} photons s^{-1} corresponding to a ZAMS star of spectral type B2. The core is associated with a methanol (MMB G339.682−01.207; Caswell 2009) and OH (OH 339.684−01.21) masers, both of which are tightly correlated with the peak of the submillimetre emission (angular offsets are smaller than the positional uncertainties).

The core MM2 is located towards the centre of the AT-LASGAL clump and is associated with an methanol maser (MMB G339.681−01.208) and so is likely hosting a young high-mass star. Analysis of the 18 GHz map reveals two radio sources, the bright radio source associated with MM3 discussed in the previous paragraph, and a second weaker radio source (G339.6804−1.2081) with a peak flux of 0.46 mJy and an SNR of 7.1. This source was not detected in the 24 GHz radio map ($f_{24GHz} < 0.5$ mJy; 3σ upper limit) and was considered a low-reliability detection and was therefore not included in our analysis. However, the tight positional correlation of this radio source with the centre of MM2 and the methanol maser has strengthened its reliability and so we include it in the discussion of this region. The 24 GHz flux upper limit is similar to the 18 GHz flux and so we can assume it is optically thin at both bands. Using this we have determined the Lyman flux to be 3.7×10^{44} photons s^{-1} corresponding to a ZAMS star of spectral type B2.

This high-mass dense clump contains three compact cores. The most massive core is mid-infrared quiet, while the two lower mass cores are both associated with embedded H II regions and OH and methanol masers. Similarly to the first clump discussed

in this subsection this would appear to be hosting a young protocluster.

This work allows us to further characterize the nature of the most massive deeply embedded sources of the SPARKS sample. Csengeri et al. (2017b) identified these sources as mid-infrared quiet clumps based on mid-infrared emission and luminosity arguments, which could host deeply embedded (proto)stars with masses corresponding to B0.5 or later main-sequence stars. Our analysis shows that the most massive deeply embedded objects are B2-B0.5-type main-sequence stars, providing independent confirmation to the initial classification by Csengeri et al. (2017b).

5 SUMMARY AND CONCLUSIONS

We have carried out high-resolution ($\sim$0.5-arcsec) and high-frequency (18−24-GHz) ATCA observations towards a sample of young H II regions that were selected on the basis of being unresolved and optically thick between 5 and 23.7 GHz with associated methanol masers. The observations were made using the 6A antenna configuration and provide continuum coverage from 17 to 25 GHz. The main aim of this work is to identify and confirm new HC H II regions based on the hypothesis that methanol masers are an excellent tracer of young and embedded high-mass stars. From the 39 observed fields, we successfully identified 27 reliable radio detections above 3σ. Utilizing various archival multiwavelength radio-data sources (such as CORNISH-North, CORNISH-South, MAGPIS, and THOR), we
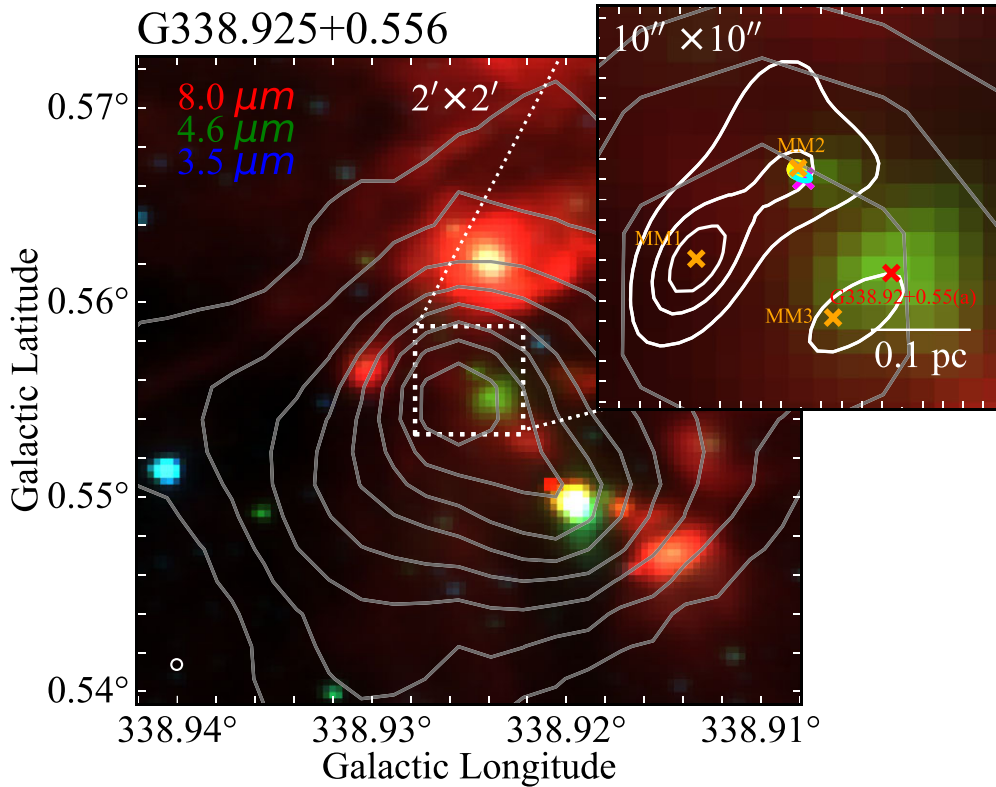
Figure 19. Three-colour composite images from GLIMPSE 8-μm (red), 4.6-μm (green), and 3.5-μm (blue) bands for HC H II region G339.884−1.25. The 870-μm dust emission from ATLASGAL is traced by the grey contours. In the upper right zoomed panel, the cyan ellipse shows the position of the high-frequency (24-GHz) radio source and the magenta cross shows the position of the MMB methanol maser. The position of the OH maser is shown as a yellow circle. The SPARKS 1.3-mm dust continuum emission is traced by white contours and the centres of the three cores identified by Csengeri et al. (2017a) are indicated by orange crosses and labelled MM1, MM2, and MM3 accordingly. The red cross shows the peak position of EGOs as identified in Cyganowski et al. (2008).

constructed SEDs between 5 and 24 GHz, where available. These SEDs allowed us to derive physical properties, including size, electron density (n_e), emission measure, Lyman continuum photon flux (N_{Ly}), and turnover frequency (ν_t), assuming an ionization-bounded H II region with a uniform electron density model. We have identified 13 HC H II regions, six transition objects, six UC H II regions, and one radio jet candidate based on their physical parameters and mid-infrared environments. The majority of these are newly reported in the work and one source is mid-infrared dark at 24 μm.

Our main findings are as follows:

(i) We identify a total of 20 HC H II regions and intermediate objects located between the class of HC H II and UC H II regions, thereby increasing the previously known sample size by ∼80 per cent.

(ii) The youngest H II regions are deeply embedded with dusty clumps and are found to be associated with a variety of masers, molecular outflows, and EGOs, all of which are excellent probes of the final stages of massive star formation.

(iii) The HC H II regions identified in this study surround younger and less massive stars. Our observations are specifically targeted towards sites of methanol masers, as they are more sensitive to lower luminosity sources. Approximately 70 per cent of our sample is associated with a methanol maser within 3 arcsec. 15 per cent of our HC H II regions do not have a methanol-maser counterpart. Our observational approach targeted towards methanol masers proves to be an effective method for identifying HC H II regions of massive star formation.

(iv) There are three HC H II regions and one HC H II/Jet candidate that remain optically thick at 24 GHz in this study; these sources are considered to be the youngest in our sample. These regions show signs of active accretion within the presence of ionized gas, suggesting the protostellar objects exciting the HC H II regions will ultimately become more massive.

In this study we observed a sample of compact H II regions selected from 141 methanol masers and successfully identified 14 HCH II regions and six transition objects constituting approximately 15 per cent of the total sample. Extrapolating these results to the remaining sample of 831 methanol masers (Caswell 2010), we can anticipate identifying approximately 170 new young and compact H II regions. While the exact number of detections depends on various factors, this scenario highlights the effectiveness of our observational approach and contributes significantly to increasing the sample of HC H II regions and to the comprehensive understanding of high-mass star formation.
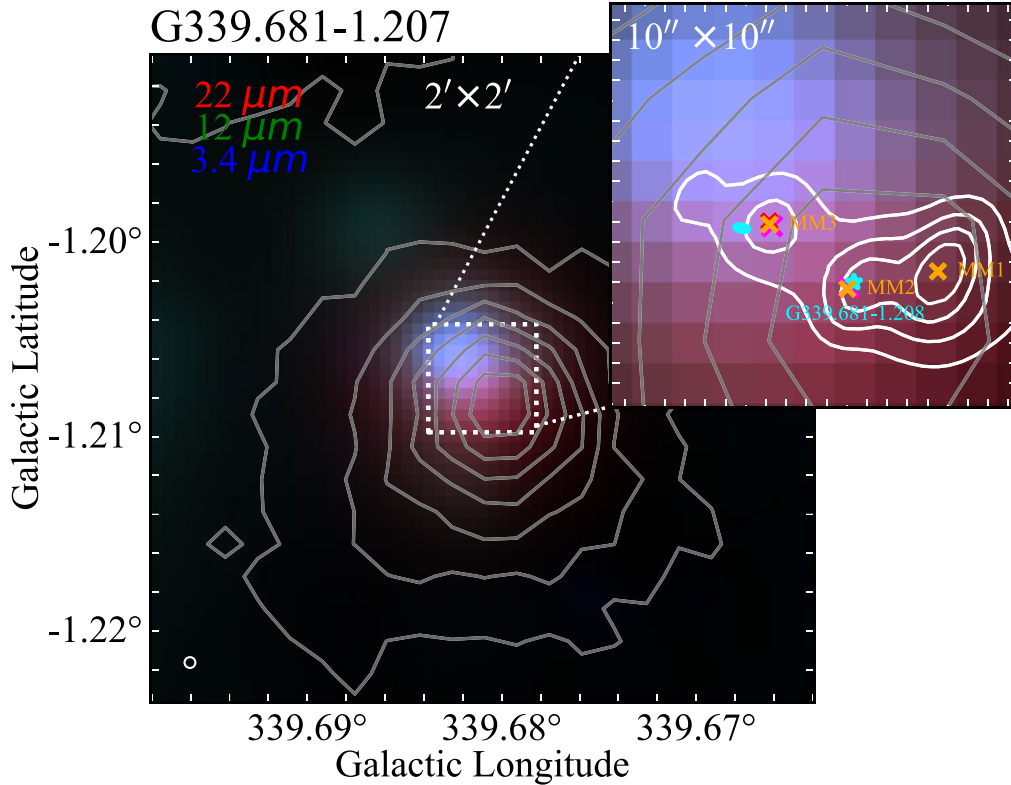
Figure 20. Three-colour composite images from WISE 22-μm (red), 12-μm (green), and 3.4-μm (blue) bands for HC H II region G339.681−1.207. The 870-μm dust emission from ATLASGAL is traced by the grey contours. In the upper right zoomed panel, the cyan ellipse shows the position of the high-frequency (24-GHz) radio source and the magenta crosses show the position of the MMB methanol maser. The OH masers is shown as a red cross. The cyan star shows the position of the marginal radio source at 18 GHz. The SPARKS 1.3-mm continuum emission is traced by white contours and the centres of the three cores identified by Csengeri et al. (2017a) are indicated by orange crosses and labelled MM1, MM2, and MM3 accordingly.

DATA AVAILABILITY

The data underlying this article are available in the article and in its online supplementary material. The full version of Table 2 is available on CDS. Copies of the SEDs and 18 and 24 GHz radio maps are available in the appendix.

REFERENCES

Afflerbach A., Churchwell E., Acord J. M., Hofner P., Kurtz S., Depree C. G., 1996, ApJS, 106, 423
Becker R. H., White R. L., Helfand D. J., Zoonematkermani S., 1994, ApJS, 91, 347
Beuther H. et al., 2019, A&A, 628, A90
Billington S. J., Urquhart J. S., Figura C., Eden D. J., Moore T. J. T., 2019, MNRAS, 483, 3146
Breen S. L., Ellingsen S. P., 2011, MNRAS, 416, 178
Breen S. L., Ellingsen S. P., Caswell J. L., Green J. A., Fuller G. A., Voronkov M. A., Quinn L. J., Avison A., 2011, ApJ, 733, 80
Breen S. L., Ellingsen S. P., Contreras Y., Green J. A., Caswell J. L., Stevens J. B., Dawson J. R., Voronkov M. A., 2013, MNRAS, 435, 524
Brown R. L., Lockman F. J., Knapp G. R., 1978, ARA&A, 16, 445
Carpenter J. M., Snell R. L., Schloerb F. P., 1990, ApJ, 362, 147
Caswell J. L., 2009, Publ. Astron. Soc. Aust., 26, 454
Caswell J. L. e., 2010, MNRAS, 404, 1029
Caswell J. L., Vaile R. A., Ellingsen S. P., Whiteoak J. B., Norris R. P., 1995, MNRAS, 272, 96

Chandler C. J., Scoville N. Z., Carlstrom J. E., 1993, in Kwok S., ed., ASP Conf. Ser. Vol. 41, Astronomical Infrared Spectroscopy: Future Observational Directions. Astron. Soc. Pac., San Francisco, p. 215
Chibueze J. O. et al., 2017, ApJ, 836, 59
Claussen M. J., 2002, in Migenes V., Reid M. J., eds, Proc. IAU Symp. 206, Cosmic Masers: From Proto-Stars to Black Holes. Kluwer, Dordrecht, p. 27
Contreras Y. et al., 2013, A&A, 549, A45
Csengeri T. et al., 2017a, A&A, 600, L10
Csengeri T., Bontemps S., Wyrowski F., Megeath S. T., Motte F., Sanna A., Wienen M., Menten K. M., 2017b, A&A, 601, A60
Cyganowski C. J. et al., 2008, AJ, 136, 2391
Davies B., Hoare M. G., Lumsden S. L., Hosokawa T., Oudmaijer R. D., Urquhart J. S., Mottram J. C., Stead J., 2011, MNRAS, 416, 972
Dawson J. R. et al., 2014, MNRAS, 439, 1596
De Buizer J. M., Walsh A. J., Piña R. K., Phillips C. J., Telesco C. M., 2002, ApJ, 564, 327
Dyson J. E., Williams D. A., 1980, Physics of the Interstellar Medium. Manchester Univ. Press, Manchester, UK
Dyson J. E., Williams D. A., 1997, The Physics of the Interstellar Medium. Manchester Univ. Press, Manchester, UK
Dyson J. E., Williams R. J. R., Redman M. P., 1995, MNRAS, 277, 700
Elitzur M., Hollenbach D. J., McKee C. F., 1992, ApJ, 394, 221
Frail D. A., Mitchell G. F., 1998, ApJ, 508, 690
Garay G., Lizano S., 1999, PASP, 111, 1049
Gaume R. A., Goss W. M., Dickel H. R., Wilson T. L., Johnston K. J., 1995, ApJ, 438, 776
Giveon U., Becker R. H., Helfand D. J., White R. L., 2005, AJ, 129, 348
Green J. A. et al., 2009, MNRAS, 392, 783

Green J. A. et al., 2010, MNRAS, 409, 913

He Y.-X. et al., 2016, MNRAS, 461, 2288

Hoare M. G., Kurtz S. E., Lizano S., Keto E., Hofner P., 2007, in Reipurth B., Jewitt D., Keil K., eds, Protostars and Planets V. University of Arizona Press, Tucson, p. 181

Hosokawa T., Omukai K., 2009, ApJ, 691, 823

Hosokawa T., Yorke H. W., Omukai K., 2010, ApJ, 721, 478

Ilee J. D. et al., 2013, MNRAS, 429, 2960

Irabor T. et al., 2023, MNRAS, 520, 1073

Kalcheva I. E., Hoare M. G., Urquhart J. S., Kurtz S., Lumsden S. L., Purcell C. R., Zijlstra A. A., 2018, A&A, 615, A103

Keto E., 2007, ApJ, 666, 976

Krishnan V. et al., 2015, ApJ, 805, 129

Kurtz S. E., 2000, in Arthur S. J., Brickhouse N. S., Franco J., eds, Revista Mexicana de Astronomia y Astrofisica Conference Series, Vol. 9, Revista Mexicana de Astronomia y Astrofisica Conference Series. p. 169

Kurtz S., Hofner P., 2005, AJ, 130, 711

Kurtz S., Churchwell E., Wood D. O. S., 1994, ApJS, 91, 659

Kurtz S. E., Watson A. M., Hofner P., Otte B., 1999, ApJ, 514, 232

Liu M. et al., 2019, ApJ, 874, 16

Lockman F. J., 1979, ApJ, 232, 761

Lumsden S. L., Hoare M. G., Urquhart J. S., Oudmaijer R. D., Davies B., Mottram J. C., Cooper H. D. B., Moore T. J. T., 2013, ApJS, 208, 11

Martins F., Schaerer D., Hillier D. J., 2005, A&A, 436, 1049

McKee C. F., Tan J. C., 2003, ApJ, 585, 850

Mezger P. G., Henderson A. P., 1967, ApJ, 147, 471

Molinari S. et al., 2010, A&A, 518, L100

Murphy T., Cohen M., Ekers R. D., Green A. J., Wark R. M., Moss V., 2010, MNRAS, 405, 1560

Panagia N., 1973, AJ, 78, 929

Patel A. L. et al., 2023, MNRAS, 524, 4384 (Paper I)

Peretto N., Fuller G. A., 2009, A&A, 505, 405

Peters T., Banerjee R., Klessen R. S., Mac Low M.-M., Galván-Madrid R., Keto E. R., 2010, ApJ, 711, 1017

Purcell C. R. et al., 2013, ApJS, 205, 1

Purser S. J. D. et al., 2016, MNRAS, 460, 1039

Purser S. J. D., Lumsden S. L., Hoare M. G., Kurtz S., 2021, MNRAS, 504, 338

Qiao H.-H. et al., 2020, ApJS, 247, 5

Reach W. T. et al., 2006, AJ, 131, 1479

Rodgers A. W., Campbell C. T., Whiteoak J. B., 1960, MNRAS, 121, 103

Rubin R. H., 1968, ApJ, 154, 391

Sánchez-Monge et al., 2013, A&A, 557, A94

Sault R. J., Teuben P. J., Wright M. C. H., 1995, in Shaw R. A., Payne H. E., Hayes J. J. E., eds, ASP Conf. Ser. Vol. 77, Astronomical Data Analysis Software and Systems IV. Astron. Soc. Pac., San Francisco, p. 433

Schuller F. et al., 2009, A&A, 504, 415

Sevenster M. N., Chapman J. M., Habing H. J., Killeen N. E. B., Lindqvist M., 1997, A&AS, 124, 509

Sewilo M., Watson C., Araya E., Churchwell E., Hofner P., Kurtz S., 2004, ApJS, 154, 553

Sobolev A. M., Deguchi S., 1994, ApJ, 433, 719

Spitzer L., 1978, Physical Processes in the Interstellar Medium. A Wiley-Interscience Publication, Wiley, New York

Titmarsh A. M., Ellingsen S. P., Breen S. L., Caswell J. L., Voronkov M. A., 2016, MNRAS, 459, 157

Urquhart J. S., Busfield A. L., Hoare M. G., Lumsden S. L., Clarke A. J., Moore T. J. T., Mottram J. C., Oudmaijer R. D., 2007a, A&A, 461, 11

Urquhart J. S., Busfield A. L., Hoare M. G., Lumsden S. L., Clarke A. J., Moore T. J. T., Mottram J. C., Oudmaijer R. D., 2007b, A&A, 461, 11

Urquhart J. S. et al., 2013a, MNRAS, 431, 1752

Urquhart J. S. et al., 2013b, MNRAS, 435, 400

Urquhart J. S., Figura C. C., Moore T. J. T., Hoare M. G., Lumsden S. L., Mottram J. C., Thompson M. A., Oudmaijer R. D., 2014a, MNRAS, 437, 1791

Urquhart J. S. et al., 2014b, A&A, 568, A41

Urquhart J. S. et al., 2015, MNRAS, 446, 3461

Urquhart J. S. et al., 2018, MNRAS, 473, 1059

Urquhart J. S. et al., 2022, MNRAS, 510, 3389

Wang Y. et al., 2018, A&A, 619, A124

Wheelwright H. E., de Wit W. J., Oudmaijer R. D., Hoare M. G., Lumsden S. L., Fujiyoshi T., Close J. L., 2012, A&A, 540, A89

White R. L., Becker R. H., Helfand D. J., 2005, AJ, 130, 586

Wilson W. E. et al., 2011, MNRAS, 416, 832

Wilson T. L., Rohlfs K., Hüttemeister S., 2013, in Wilson T. L., Rohlfs K., Huttemeister S., eds, Tools of Radio Astronomy. Springer Berlin Heidelberg, Berlin, NY

Wood D. O. S., Churchwell E., 1989, ApJ, 340, 265

Yang A. Y., Thompson M. A., Tian W. W., Bihr S., Beuther H., Hindson L., 2019, MNRAS, 482, 2681

Yang A. Y. et al., 2021, A&A, 645, A110

Yang A. Y. et al., 2023, preprint (arXiv:2310.09777)

Zhang M., Kainulainen J., Mattern M., Fang M., Henning T., 2019, A&A, 622, A52

SUPPORTING INFORMATION

Supplementary data are available at *MNRAS* online.

Appendix A. Excluded radio maps.
Appendix B. Radio SED.
Appendix C. Mid Infrared Environments of Hc H Regions.
Appendix D. Radio Maps of all Detections.
Table 2. Observational parameters from all observed fields.

Please note: Oxford University Press is not responsible for the content or functionality of any supporting materials supplied by the authors. Any queries (other than missing material) should be directed to the corresponding author for the article.

This paper has been typeset from a TEX/LATEX file prepared by the author.